INVESTIGATION OF ABLATION OF ICE BODIES IN HYPERSONIC FLOWS

Thesis by

David E. Anderson

In Partial Fulfillment of the Requirements
For the Degree of
Aeronautical Engineer

California Institute of Technology
Pasadena, California
1960

ACKNOWLEDGMENTS

The author wishes to express his appreciation to Professor Lester Lees whose groundwork for this investigation was invaluable, and to Professor Toshi Kubota for the great amount of time, energy, and expert guidance expended in the research. He is grateful to Mr. Paul Baloga and members of the hypersonics staff for suggestions and assistance in all phases of model preparation and test; to Mr. C. A. Bartsch and members of the GALCIT machine shop for the careful production of models and test devices; to Mrs. Betty Laue and Miss Georgette Pauwels for the computing; to Mrs. Betty Wood and Mrs. Nell Kindig for preparation of the figures; and to Mrs. Geraldine Van Gieson for the excellent typing of the manuscript.

ABSTRACT

The physical characteristics of the ablation process are described. A theoretical approach to calculate the heat transfer to the wall of an ablating body under flow conditions encountered in the GALCIT hypersonic tunnels is outlined. Simplification is achieved by assuming the vapor pressure next to the subliming body is at its equilibrium value. The GALCIT hypersonic test facilities are described briefly. Methods of manufacture are given for CO_2-ice, H_2O-ice, and $C_{10}H_{16}O$-ice models. Techniques and special test equipment used in obtaining experiments results with H_2O-ice and $C_{10}H_{16}O$-ice (camphor) are described. An illustration of the computational technique used to determine the heat transfer rates to the wall and the wall temperature distributions is included. Figures to show the agreement between theory and experiment are presented and reasonable results are obtained for temperature distribution, but heat-transfer rates (ablation rates) are greater for theory than for experiment.

TABLE OF CONTENTS

LIST OF FIGURES

LIST OF SYMBOLS

B	$\frac{\dot{m}_i}{\rho_e u_e C_{H_O}}$	mass addition parameters
B'	$\frac{\dot{m}_i}{\rho_e u_e C_H}$	
C_f	skin friction coefficient	
C_H	local Stanton number, $\frac{\dot{q}_w}{\rho_e u_e (h_{s_e} - h_{A_w})}$	
c_p	specific heat at constant pressure	
D	diameter of body	
D_{12}	coefficient of mass diffusion of species 1 into species 2	
(g)	in the gas phase	
h_s	stagnation enthalpy	
Δh_s	$h_{s_e} - h_{A_w}$	
H	effective heat capacity	
k	coefficient of thermal conductivity	
K_E	mass fraction of subliming material	
K_i	mass fraction of the i^{th} species	
Le	Lewis-Semenov number, $\frac{\rho D_{12} c_p}{k}$	
L_V	latent heat of sublimation	
L_T	internal heat capacity of solid material up to sublimation temperature	

$\dot{m}$	rate of mass addition to the boundary layer
M	Mach number , $\frac{\text{local stream velocity}}{\text{velocity of sound}}$
Nu	Nusselt number, $(\rho_e/\rho_w)\, C_H \cdot Re \cdot Pr$
p	static pressure
p_o'	stagnation pressure behind normal shock
p_v	vapor pressure of the subliming material
Pr	Prandtl number, $(c_p\, \mu)/k$
$\dot{q}$	local heat transfer rate
$\dot{q}_s$	net heat transfer rate to interior of solid
r	radius of curvature at nose of body
R	radius of cross-section of body of revolution
R_o	universal gas constant
Re_s	Reynolds number , $\frac{\rho\, u_e\, s}{\mu}$
R_{e_∞}	free stream Reynolds number per unit length , $\frac{\rho_\infty\, u_\infty}{\mu_\infty}$
(s)	in the solid phase
s	distance along surface, measured from forward stagnation point
Sc	Schmidt number, $(\mu/\rho D_{12})$
t	time
T	absolute temperature
T_o	recovery temperature
u, v	components of velocity parallel and normal to gas-solid interface
w_a	axial ablation velocity
W_i	molecular weight of the i^{th} species
x	axial distance, measured from nose
y	distance normal to interface

β	slope of curve $C_{H_O}/C_H = 1 + \beta B'$
μ	absolute viscosity
ρ	density
θ	angular distance from the nose

Subscripts

A	air or gas composing free stream flow
e	flow quantities evaluated at outer edge of gas boundary layer
E	solid material
o	zero mass addition; also reservoir value
s	solid
s. p.	stagnation point
w	wall
∞	free stream ahead of bow shock wave

I. INTRODUCTION

Ablation is the process whereby a body absorbs heat by giving up part of its mass, either by melting with or without evaporation, or by direct sublimation from the solid state. Ablation similar to the type considered in this report is found most commonly in nature in the form of meteorites which enter the earth's atmosphere at high velocity and generally (if they are neither too large nor too small) vaporize before they strike the ground.* Ablation shows promise as an engineering weapon against high heat transfer rates and high material temperatures in several applications, the most obvious being for nose cones of ballistic missiles, or other bodies entering the earth's atmosphere. Lees[2] points out that the heat transfer rate at the throat of liquid fuel rocket nozzles can be as high as 1000 BTU/ft.^{2} sec., and values of the order of 2500 - 3000 BTU/ft.^{2} sec. may be reached at the forward stagnation point of ballistic missiles during reentry.

Sublimation ablation or melting ablation where a significant portion of the molten material is vaporized offers a reduction in the heat transfer rate to the body for two general reasons:

(1) Absorption of a significant portion of the incident heat in latent heat of sublimation (evaporation) of the body material.

(2) Insulation of the body by its own vapor in the boundary layer.

Consider a semi-infinite slab of material subjected to an impulsive constant heat transfer at the surface.**If the temperature, the

---

* Sin-I Cheng[1] presents some interesting comments on and photographs of meteoric ablation. (Superscripts denote references at the end of the text.)

** Lees[2] points out that a triangular timewise distribution of heat transfer rate is a good approximation to the heat pulse during reentry.

distance from the surface, the time, and the heat flux are denoted by T, X, t and for $\dot{q}_w$ respectively, then

$$T(X,\ t) = \frac{\dot{q}_w}{\kappa} \left\{ \sqrt{(\kappa t/\pi)} \ e^{\frac{-\rho c X^2}{4kt}} - X \ \operatorname{erfc} \left(\frac{X}{2} \sqrt{(\rho c/kt)} \right) \right\}$$

where ρ, c, k, and κ, are respectively the density, specific heat, thermal conductivity and thermal diffusivity of the solid material, and erfc (z) denotes the complementary error function. In particular, at the surface X = 0, the temperature is given by

$$T(0,\ t) = \frac{\dot{q}_w}{\sqrt{\pi \rho c k}} \sqrt{t} \quad ,$$

and hence, even in the case of a material with high conductivity and heat capacity, there is a limit to the heat transfer rate that maintains surface temperatures below the fusion point of the material involved. When the material begins to melt at the surface, a certain amount of heat is absorbed in changing the phase of the material from solid to liquid and the heat transfer into the solid is reduced by that amount. (This does not apply to amorphous materials which do not have a sharp melting temperature.) If the liquefied material is convected away from the melting region and resolidifies in the region of low heat transfer rate or in the wake, namely if aerodynamic ablation occurs, the melted material acts as an agent which redistributes or reduces the heat transfer to the solid body. Sublimation ablation offers a particularly good means of regulating surface temperatures to tolerable levels because of the heat blocking effect of the ablated material and absorbtion of heat by the latent heat of sublimation. Also as seen by the Clausius-

Clapeyron equation for vapor pressure

$$\log_e p_v = -(L_v/R_o T) + Q$$

where Q = constant, an increase in T will result in an increase in p_v and hence the heat absorption and blockage effect by blowing will be increased until a balance is achieved. By this mechanism, the ablation process is self-regulating. In addition the vapor pressure curve versus temperature is so steep that theoretically one has only to find a suitable material to regulate the maximum temperature experienced to a given level. Further, as shown by Adams[3] for applications such as recovery of a satellite the required weight for an ablating nose cone may be less than for a radiating nose cone when the required weight for insulation is considered. Schemes where a gas is ejected at the nose of a body have the disadvantage of excess weight and mechanical complexity of pumps, regulating devices, and plumbing.

Lees[2, 4, 5], Kubota[6], Bethe[7] and Adams, Fay[8] and Riddell, Roberts[9], and others have worked out the theory for the heat transfer rate to bodies in hypersonic flow including the effects of ionization, dissociation, combustion in the boundary layer, recombination, radiation from the hot gases behind the bow shock and back radiation from the body. By specializing these general results to the conditions existing in the GALCIT hypersonic tunnels*, it is possible to obtain theoretical results which may be used to predict the salient macroscopic parameters of

---

* See page 10 for a brief description of the GALCIT hypersonic facilities.

temperature, heat transfer rate, and ablation rate for a given material, model shape, and tunnel operating conditions. These results are based on well understood fluid mechanical aspects of the problem and allow the experimental results obtained to serve as a check on the portions of the theory still retained. Since the flow conditions in hypersonic tunnels of the GALCIT type are now well known, it is hoped that these results will prove an interesting supplement to the results obtained in high energy sources such as air arc jets and rocket exhausts where high enthalpies are obtained, but where flow conditions are less well known.

II. THEORY OF HEAT TRANSFER TO ABLATING BODIES

II. 1. Concentration and Stagnation Enthalpy Distributions in the Boundary Layer, Le = Pr = Sc = 1

Lees[5] shows that for flows of boundary layer type where Le = Pr = Sc = 1, K_A and h_s satisfy identical differential equations.* Hence, if the boundary conditions imposed on K_A and h_s at the wall and at the edge of the boundary layer are compatible, and K_{A_w} and h_{s_w} are slowly varying along the body surface, then the distributions of h_s and K_A will be similar. Based on this fact, the conservation of mass for each chemical species, and defining

$$\left\{ k\,(\partial T/\partial y) + \rho\, D_{12} \sum_i h_i\,(\partial K_i/\partial y) \right\}_w = \rho_e\, u_e\, C_H\,(h_{s_e} - h_w) \quad ,$$

one obtains

$$K_{E_w} = B'/(B' + 1)$$

or

$$B' = (K_{E_w})/(1 - K_{E_w}) \qquad (1)$$

where

$$B' = \dot{m}/(\rho_e\, u_e\, C_H) \quad .$$

Also it is shown in Section II. 2. that

$$\dot{m}(L_V + L_T) = \rho_e\, u_e\, C_H\,(h_{s_e} - h_{A_w}) \quad .$$

Combining Eq. (1) and the above relations yields

---

* Note that $K_E = 1 - K_A$.

$$B' = \frac{(h_{s_e} - h_{A_w})}{L_V + L_T} \quad . \tag{2}$$

Assuming that the vapor pressure of the solid material is at its thermodynamic equilibrium value

$$K_E = \frac{W_E\ p_v}{W_A\ (p - p_v) + W_E\ p_v}$$

and Eq. (1) becomes

$$B' = (W_E/W_A)\left(\frac{p_v/p}{1 - \frac{p_v}{p}} \right) \quad . \tag{3}$$

Figures 1 through 3 were prepared by T. Kubota^6 from Eqs. (2) and (3), taking $(h_{s_e} - h_{A_w}) = c_{p_A}(T_o - T_w)$, $L_T = 0$, and using the Clausius-Clapeyron vapor pressure equation. With figures such as 1 through 3 for a particular wall material, the equilibrium wall temperature can immediately be determined once the recovery temperature and pressure distribution are known.

II. 2. Heat Transfer Normal to Streamlines in Boundary Layer Flows

For steady state conditions there will exist a heat transfer balance

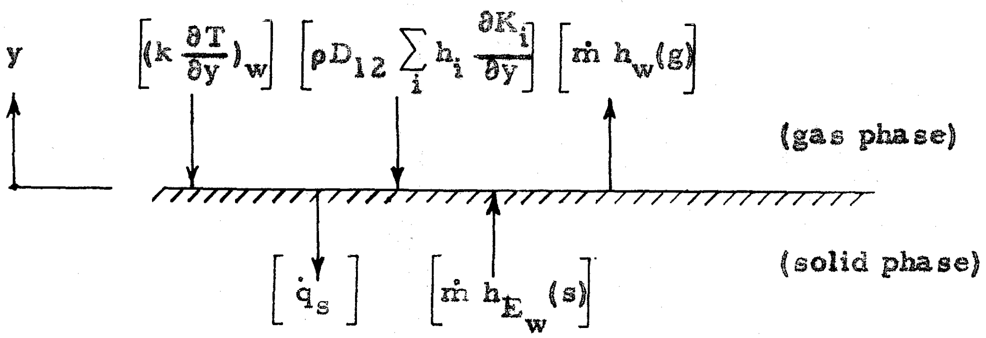

at the surface of any body immersed in a fluid. Consider an ablating gas-solid interface with coordinates fixed in the interface.

In the gas phase there are three terms to be considered for the heat transfer at the wall:* (1) conduction to the wall, $(k \frac{\partial T}{\partial y})_w$; (2) diffusion of different species to the wall carrying their associated enthalpy, $(\rho D_{12} \sum_i h_i \frac{\partial K_i}{\partial y})_w$; (3) blowing of material away from the wall = $\dot{m} h_w (g)$.

In the solid phase there are two terms to be considered for the heat transfer at the wall: (1) conduction of heat into the interior of the solid, $\dot{q}_s$; (2) convection of enthalpy to the wall (since the coordinates are fixed in the interface), $\dot{m} h_{E_w} (s)$.

Hence balancing heat to the wall in the gas = heat away from the wall in the solid

$$\left[k \frac{\partial T}{\partial y} + \rho D_{12} \frac{\partial K_A}{\partial y} (h_A - h_E)\right]_w - \dot{m} h_w (g) = \dot{q}_s - \dot{m} h_{E_w} (s) \qquad (4)$$

define

$$\rho_e u_e C_H \left[h_{s_e} - h_w(g)\right] = k \frac{\partial T}{\partial y} + \rho D_{12} \sum_i h_i \frac{\partial K_i}{\partial y} \qquad (5)$$

but

$$h_w(g) = \left[\sum_i K_i h_i\right]_w (g) = K_{E_w} h_{E_w} (g) + (1 - K_{E_w}) h_{A_w} (g) \qquad (6)$$

$$B' = \frac{\dot{m}}{\rho_e u_e C_H} = \frac{K_{E_w}}{1 - K_{E_w}}$$

---

* We ignore here radiation and chemical reactions at the wall. See Reference 5 for an accounting of the terms in the general case.

hence

$$\dot{m} = \rho_e \, u_e \, C_H \frac{K_{E_w}}{1 - K_{E_w}} \quad . \tag{7}$$

Substituting Eqs. (5), (6), and (7) in Eq. (4) and rearranging terms yields

$$\dot{q}_w = \rho_e \, u_e \, C_H \left[h_{s_e} - h_{A_w} \right] - \dot{m} \left[h_E \,(g) - h_E \,(s) \right]_w$$

where $\left[h_E \,(g) - h_E \,(s) \right]_w$ is the latent heat of sublimation L_V.

Defining $\dot{q}_s = \dot{m} \, L_T$,

$$\dot{m} \, (L_V + L_T) = \rho_e \, u_e \, C_H \, (h_{s_e} - h_{A_w}) \quad . \tag{8}$$

If $\dot{q}_w$ is taken as $\rho_e \, u_e \, C_H \, (h_{s_e} - h_{A_w})$ then

$$\dot{q}_w = \dot{m} \, (L_V + L_T) \ .$$

In order to obtain results that will allow use of pioneering work by other authors[10] in computing the heat transfer parameter, one can define

$$C_H = (\rho_w / \rho_e) \left[\frac{Nu}{Pr \, Re_s} \right]_w$$

then

$$\dot{q}_w = \rho_w \, u_e \left[\frac{Nu}{Pr \, Re_s} \right]_w (h_{s_e} - h_{A_w})$$

$$\dot{q}_w = \sqrt{\frac{\rho_w \quad _w \, u_e}{s}} \left[\frac{Nu}{Pr \sqrt{Re_s}} \right]_w c_{p_A} \, (T_o - T_w) \quad . \tag{9}$$

The case of melting ablation is not considered here. In the case of body materials of high latent heat of sublimation and/or low conductivity, it is possible to ignore heat conduction into the solid and take

$$\dot{m}\, L_V = \dot{q}_w \quad . \tag{10}$$

This assumption was used to analyze the ablation data for these tests. An estimate is made in Appendix C of the error involved in considering $L_T = 0$.

II. 3. Blowing Correction for Heat Transfer

Defining $\dot{q}_w$ for zero mass transfer as

$$(\dot{q}_w)_{\dot{m}=o} = \rho_e\, u_e\, C_{H_O}\, (h_{s_e} - h_{A_w})$$

gives immediately that

$$\frac{(\dot{q}_w)_{\dot{m}\neq 0}}{(\dot{q}_w)_{\dot{m}=0}} = C_H/C_{H_O} \quad .$$

Theoretical considerations[11] indicate that the equation for C_H/C_{H_O} is of the form

$$C_H/C_{H_O} = \frac{1}{1 + \beta\, B'} \quad . \tag{11}$$

Correlating theoretical and experimental results for mass addition into a laminar boundary layer, T. Kubota determined the value of β as $\beta = 0.84\, (W_A/W_E)^{1/3}$. The experimental and theoretical results mentioned in this correlation are based on body materials in which $2 \leqq W_E \leqq 44$.

An effective heat of sublimation can be defined by

$$H = L_V \frac{(\dot{q}_w)_{\dot{m}=0}}{(\dot{q}_w)_{\dot{m}\neq 0}}$$

$$H = L_V\, (1 + \beta\, B') \tag{12}$$

$$H = L_V + \beta\ \Delta h_s \quad .$$

Hence the effective heat of sublimation increases linearly with stagnation enthalpy difference across the boundary layer.

III. EXPERIMENTAL INVESTIGATION

III. 1. Introduction

The experimental investigation of subliming ablation was conducted in the GALCIT hypersonic wind tunnels. The models used in the experiments were hemisphere-cylinders of 1-inch diameter made of H_2O-ice, $C_{10}H_{16}O$-ice, and CO_2-ice. In the first phase of the investigation, the models were tested at wide ranges of temperature and pressure in order to explore the general behavior of these materials in hypersonic air streams. (See Section III. 5.) In the second phase of the investigation, the temperature distributions and the rates of ablation were measured on H_2O-ice and $C_{10}H_{16}O$-ice models. In the third phase of the investigation, a study of the equilibrium shapes of ablating bodies was conducted with H_2O-ice and $C_{10}H_{16}O$-ice models initially of hemisphere-cylinder shape. In addition to the ablation models, two metal pressure models were machined with orifices distributed on the surface; one model was of hemisphere-cylinder shape, and the other of the "equilibrium" shape obtained with a camphor model. From the measured pressure distributions the ablation rates were computed by the method outlined in Section II. and compared with experimental values.

III. 2. Wind Tunnels

The experiments were performed in the GALCIT hypersonic wind tunnels legs 1 and 2. Both tunnels are of the continuous running closed return type, and are supplied by the same compressor plant, hence they are run alternately. The design features of these two tunnels are set forth in the following table:

	Leg 1	Leg 2
Mach No. Range	5.8 (mean)	6 to 10
Max. Reservoir Temp., °C	149	867
Max. Reservoir Pressure, psig	100	300
Test Section, Dimensions, In.	5 x 5	7.1 x 7.3

Leg 1 is a fixed contour nozzle and leg 2 is a variable contour nozzle with ten pairs of hand-operated jacks. (See Figure 4.) Leg 2 is a complete operating 3/8 scale model of the 21 x 21 inch hypersonic tunnel at the Caltech Jet Propulsion Laboratory. Both legs 1 and 2 feature automatic control of the reservoir temperature and pressure. The temperatures are maintained by nichrome wire electrical-resistance heaters immediately preceding the test sections.

III. 3. Model Support and Shield

Because of the high temperatures encountered in the GALCIT leg 2 hypersonic tunnel it is necessary to bring the tunnel airflow up to temperature while the wind is blowing; also flow had to be started at much higher pressures than were used for these tests. Hence in order to preserve bodies with low melting points or high vapor pressure character, such as H_2O-ice or solid camphor ($C_{10}H_{16}O$), it was mandatory to protect the models from the airstream. This was accomplished by withdrawing the model from the airstream and holding it in a cooled protective case which could be opened and allow the model to be raised into the airstream through a cutout in the tunnel floor after the desired flow conditions had been established. The device for accomplishing this task is shown in Figure 5. Because of the high melting point of camphor and the high latent heat of H_2O-ice, it was satisfactory to cool the model with ordinary atmospheric cooling air. Had CO_2-ice or other low melting point materials been tested in leg 2, cooler temperatures could have been obtained by using liquid N_2 for the cooling medium. Cooling by means of liquid N_2 was tried in leg 1 and model temperatures on the order of -200°C were obtained. In leg 1 because of the lower reservoir temperatures, it is possible to bring the airflow up to full stagnation temperature while the tunnel air is channeled through by-pass lines and then to establish flow in the tunnel at full stagnation conditions in about one minute after model installation; hence no device for model protection was required.

III. 4. Manufacture of Models

The CO_2-ice models were first made by placing commercial dry ice in a high pressure mold with a micarta sting fixed in place. The CO_2 was allowed to melt, and was then refrozen by immersing the mold in liquid N_2 . The molds were then thawed to remove the models which often came out with considerable velocity (this can be a dangerous maneuver if one is curious enough to look down into the mold). Later CO_2-ice models were manufactured by compressing the crushed dry ice in a mold, which is a far better and safer technique.

The H_2O-ice models were the most difficult to manufacture. First the air had to be removed from a supply of distilled water by holding the water under vacuum. The solubility of O_2 and N_2 in H_2O is given by Henry's law,

$$K_i = S_t p ,$$

where K_i is concentration of the i^{th} gas species, S_t is the coefficient of solubility at a given temperature, and p is the partial pressure of the gas over the liquid. (See Figure 6 for values of K_{O_2} and K_{N_2} in H_2O.) Because of the solubility characteristics of air in water, the gas over the water to be used for the models was evacuated of air for a period of at least one day to scavenge the air from the liquid. Then the water was ejected into molds with micarta stings fixed in place, held under a vacuum and frozen (under vacuum) in an ordinary freezer. In order for this scheme to work, it is advisable to boil the water under vacuum while in the molds so that the bubbles of vapor, which have a large area, will scavenge all the air from the system. The greatest difficulty with H_2O-ice models lies in keeping the sides of the model uniform. Any slight irregularity in surface slope causes considerable variation in both pressure and pressure gradient, and hence heat transfer rate, or ablation rate, thus making it very difficult to obtain good data repeatability with this type of model. These difficulties appeared to have little effect on the surface temperature distribution, however, because of the steepness of the vapor pressure curve versus temperature.

The $C_{10}H_{16}O$-ice models were made by pressing granulated camphor under 8000 lbs. hydraulic pressure in brass molds. This method produced models of good dimensional accuracy and fairly uniform density*, and is recommended for $C_{10}H_{16}O$-ice and CO_2-ice models. The accuracy of this technique is reflected in the uniformity of ablation results for the camphor models.

To obtain model temperature data, copper-constantan thermocouples models were made (See Figure 7.), with the thermocouples fixed on the exterior of a hollow micarta sting. The thermocouple wires were lead in a circumferential direction on the micarta sting for 0.20 to 0.50 inch from the thermocouple junction in order to decrease errors caused by conduction in the thermocouple wire itself. The ice was then frozen on the stings in the case of the H_2O-ice models, or deposited in successive layers similar to a candle-making technique in the case of the $C_{10}H_{16}O$-ice models.

III. 5. Exploratory Tests: Role of the Triple Point

Exploratory tests were run in legs 1 and 2 with H_2O-ice and CO_2-ice models to examine general aspects of the ablation phenomena. The models were tested at zero angle of attack under wide conditions of temperature and pressure and were viewed by the naked eye and through a short focal length telescope. The CO_2-ice models were found to exhibit flaking on the surface and hence to lose a large share of their material by fragmentation.** For this reason and because of the difficulties of manufacture and storage of CO_2-ice models, no quantitative data were attempted with this type of model. It should also be noted (See Figures

---

* The value of the density achieved in this manner with $C_{10}H_{16}O$-ice was 4 per cent lower than the value listed in physical tables.

** Other investigators[12] using CO_2-ice models have had difficulty with fragmentation.

2 and 3.) that the values of B' achieved with CO_2-ice and $C_{10}H_{16}O$-ice are very nearly the same and therefore preclude working with both materials to spread the range of B' values attainable. The values of Δh obtained with CO_2-ice will be larger, however, because of the lower wall temperatures.

The H_2O-ice models were observed to melt at the nose in leg 1 for supply pressures greater than 34 psia at $T_o = 149°C$. If the pressure was appreciably greater than this value, a distinct crater or melt region of greater or less severity would form at the nose, depending on the magnitude of the reservoir pressure. (See Figures 8 and 9.) The reason for melting is seen from the relationship between the phases of a crystalline substance and the temperature and pressure (See sketch.).

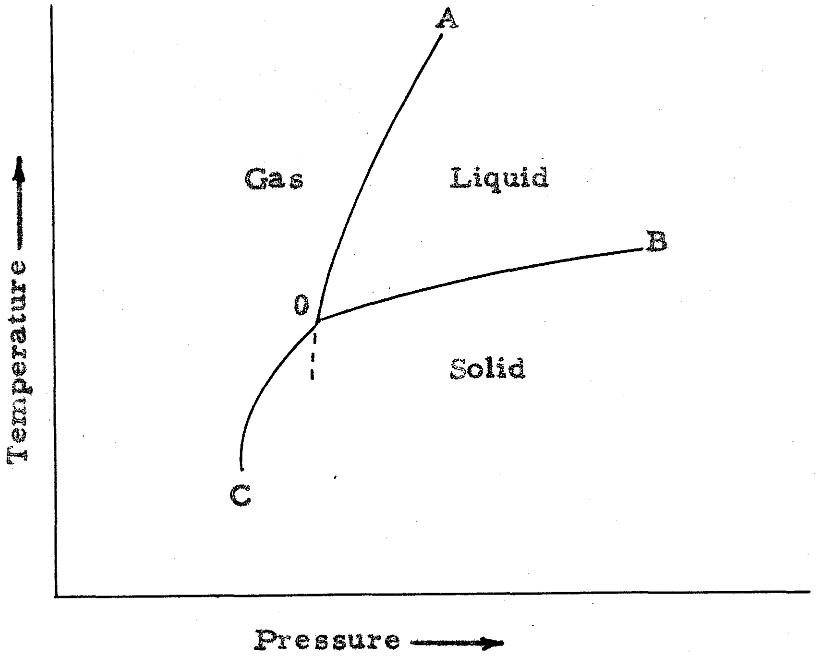

In the sketch, the locus of points OA represent the boiling temperature of the given substance in the liquid state at the corresponding pressure; the locus of points OB represents the melting conditions for the solid state; the locus of points OC gives the conditions under which the solid will sublime, and O is the triple point at which all three states may coexist. The dotted line from O represents suppression of the freezing point, or supercooling. The triple point for the most common form of H_2O-ice occurs at O°C and 0.0886 psia pressure. At a recovery temperature of 149°C in leg 1, it was found possible to hold T_w less than 0°C so long as the reservoir pressure was less than 2 atm., and melting at the nose was not apparent at pressures less than 34 psia.

Based on this simple relationship and using Figure 1, it is easy to determine the reservoir conditions of temperature and pressure which will induce stagnation point melting at any given Mach number. Because of the low viscosity of water, once the H_2O-ice melted it was convected away, thus causing the cratering effect. Melting was not a problem with any of the other materials that were tested.

III. 6. Test Conditions for Quantitative Data

Since any cratering with the models made accurate quantitative data impossible to obtain, all tests with H_2O-ice models were run at reservoir temperatures and pressures such that the model nose temperature was approximately 0°C.

The test conditions used for all quantitative data measurements on ablation rate are set forth in the following chart:

	Leg 1	Leg 2
M_∞	5.8	8.0
T_o °C	149	482
P_o atm. ($C_{10}H_{16}O$)	2.34, 3.70	5.06
P_o atm. (H_2O)	2.00	3.70
Angle of Attack	0	0

III. 7. Data Gathering Technique

To obtain quantitative data on ablation rates, time lapse photographs were taken of the model profiles with a 35 mm single-lense reflex camera fitted with a 135 mm telephoto lense with extension tube for close work. By taking a series of photographs of a model at specified time periods during a run, a time lapse series of the ablation process was obtained. The photographic images of the model were later carefully measured on an optical comparator to accuracies on the order of 0.0003 inches on the film (.001 inches absolute), giving the ablation rate at all points on the silhouette of the axially symmetric body. (See Figures 10 through 13.)

The camera was invariably positioned at least 3 feet from the 1-inch diameter model, hence the cosine error introduced in photographing the model silhouette was negligible. Errors caused by distortion in the photographic process were checked by photographing a 6-inch scale and measuring the inch marks on the film; errors from this source are deemed to have been less than 0.1 per cent.

Perhaps the largest source of error was lack of picture sharpness, caused mainly by the tunnel plate glass windows; this effect was aggravated by the oil always present in the tunnel and found on the windows after tunnel operation.

Model temperature data were recorded on a Brown self-balancing potentiometer, which was calibrated to the temperature of distilled ice slush and boiling distilled water. Because temperature gradients will exist within the material even after the wall temperature has stabilized, accurate wall temperature data are obtained only when the thermocouple is coincident with the gas-solid interface. To minimize this effect, only those temperature data which were obtained at the end of a data run were used.

Model pressure data were recorded on a precision lead-screw mercury micro-manometer for the higher pressures near the stagnation point (local body slope more than 45° to the flow direction) and a silicone oil multiple manometer bank for the pressure orifices farther back on the body. (See Figures 14 and 15.)

III. 8. Equilibrium-Shape Models

There is good reason to believe that an ablating body under conditions such as were encountered in these tests will approach an equilibrium shape, if one examines the two extremes of body shape for laminar boundary layer flow: (1) If the nose shape is highly convex or pointed (see sketch) then the maximum heat transfer and maximum ablation rate will occur at the forward stagnation point and the body will become more blunt; (2) If the nose shape is initially flat then the heat transfer and ablation

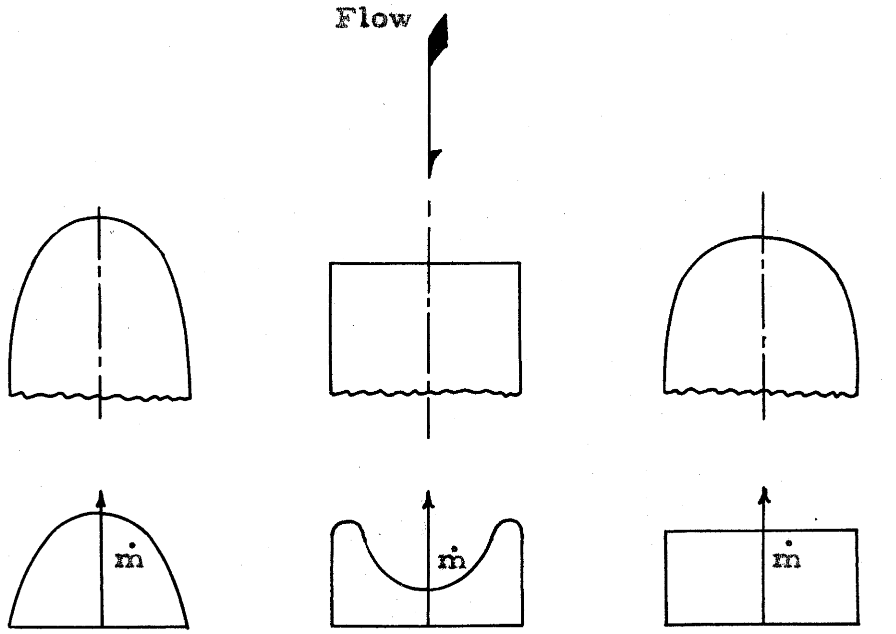

(a) Highly Convex Nose (b) Flat Nose (c) Equilibrium Shape

rates near the shoulder are larger than at the forward stagnation point. This fact can be seen from Eq. (9). If the nose is flat, then u_e will increase as the flow approaches the shoulder; also du_e/ds will increase approaching infinity at the corner.*

---

* Kemp[13], Rose, and Detra show experimentally and theoretically that the peak heat transfer rate for a flat-nosed cylindrical body with a small corner radius is reached at the shoulder and not at the forward stagnation point. Chones[14] presents experimental data to show that the heat transfer parameter, $Nu/\sqrt{Re}$, and the non-dimensional velocity, u_e/a^* , increase very rapidly as the sharp corner of a flat nose cylinder is approached.

Initially then, these two extremes in body shape will be expected to approach each other and there may exist some intermediate shape, as in the foregoing sketch. In part (c) of the sketch, the feedback between ablation and heat transfer rate has established an equilibrium, the heat transfer rate per unit cross section area is nearly constant, while the ablation rate per unit cross section area is constant.

The condition for an equilibrium shape based on simple geometrical considerations[2] is

$$(\partial R/\partial t) + w_a (\partial R/\partial x) = 0.$$

T. Kubota* has examined the determination of the equilibrium shape theoretically, assuming a modified Newtonian pressure distribution near the stagnation point, $\dot{q}_s = 0$, and using the same method of computing $(Nu/\sqrt{Re_s})_w$ as used in Reference 10. (See Appendices B and D.) His results indicate that the radius at the stagnation point increases with time. As shown in Appendix D, he also obtained the result

$$\left[\frac{1}{a^*} \frac{du_e}{d(s/r)}\right]^2 = \frac{6A + 7}{6(5 - A)} \left(\frac{\gamma + 1}{\gamma - 1} \right)$$

by assuming a linear external velocity distribution. With a*, A, and γ all known for a given material and test conditions, one can determine the value for $du_e/d(s/r)$ to fit this relationship. Assuming an ellipsoidal nose shape one can determine the ratio of the major and minor axes of the ellipsoid that will agree with this equation. For the conditions of the H_2O-ice at $P_o = 2.34$ atmospheres, $M_\infty = 5.8$, and $T_o = 149^\circ C$, his results indicate that the equilibrium ellipsoid determined by this equation

---

* Private communication.

would have its major axis perpendicular tb the flow direction and a ratio of major axis to minor axis of 4.6 to 1. For the conditions of $C_{10}H_{16}O$-ice at $P = 2.00$ atmospheres, $M_\infty = 5.8$ and $T_o = 149\ ^oC$, his results indicate that an ellipsoid with its major axis perpendicular to the flow direction, and a ratio of amjor axis to minor axis of 6.0 to 1 would be obtained. To check these ideas, H_2O-ice and $C_{10}H_{16}O$-ice models with length to diameter ratios on the order of 7 were constructed and tested in leg 1. (See Figures 12 and 13.) These models were run for 34 minutes and 39 minutes respectively to allow them to approach their equilibrium shape as closely as possible. An examination of Figures 12 and 13 indicates that the nose shapes can indeed be quite accurately approximated by oblate ellipsoids with their major axes normal to the flow direction out to the region of body slope on the order of 30 degrees to the flow direction. For the case of H_2O-ice the ratio of major axis to minor axis obtained experimentally was 1.7 to 1, and for $C_{10}H_{16}O$-ice the ratio of major axis to minor axis was 5.8 to 1. In the case of the $C_{10}H_{16}O$-ice model, a pressure model was constructed duplicating the final shape of the actual model and was tested in leg 1 to determine the pressure distribution along the surface. From these pressure data, calculations were made of the heat transfer rate and compared with the experimental values.

The pressure distributions obtained for both the hemisphere-cylinder and the equilibrium-shape models are presented in Figures 14 and 15, respectively.

IV. RESULTS AND DISCUSSION

Particular hope for the accuracy of the experimental data is derived from the excellent linearity for the ablation rates at the nose. (See Figures 16 through 20.) At the start of each test there was an adjustment period while the tunnel flow conditions and model temperature stabilized although the tunnel was run for approximately 15 minutes at full reservoir conditions before each test to decrease the effects of nozzle block temperature adjustment. These transient effects caused some anomalies to occur in the ablation rates for the first minute or two of each run. Hence, the plots of ablation rate at the nose do not include the first data points where obvious errors were involved. That is, $t = 0$ and $x = 0$ are taken at the time and nose position about 2 minutes after the start of the flow. (The ablation rate at the nose is defined as the rate at which the nose recedes with time.)

The temperature measuring system as a whole — the Brown self-balancing potentiometer and the copper-constantan thermocouples — was certainly accurate to within $\pm 1^{\circ}C$. However temperature gradients within the ablating materials caused such scatter in the experimental data that the theoretical data are considered far more reliable. (See Figures 21 through 25.) The fact that the onset of melting at the nose is predicted accurately and with good repeatability by Figure 1 in the case of H_2O-ice indicates that the actual wall temperatures were close to the theoretical predictions.

A calculation was carried out to estimate the rate of conduction of heat into the interior of the model, $\dot{q}_s$, based on the theoretical wall temperature distribution at the hemispherical nose and assuming a uniform temperature distribution over the base of the hemisphere. (See Appendix C.) However, the assumption of a uniform temperature distribution over the base of the hemisphere probably leads to higher temperature gradients at the stagnation point than would actually be achieved, and hence the estimated conduction effects at the nose might be larger than the actual effects. Experiments with the H_2O-ice models to measure the temperature difference across the micarta midway back on the body indicated that no measurable difference in temperature existed hence the conduction effects on the afterbody are presumed to be small. The accuracy of this assumption was enhanced in the case of the H_2O-ice models by the high latent heat of sublimation of ordinary ice (i.e., $L_V + L_T \cong L_V$), and in the case of the $C_{10}H_{16}O$-ice models by the low coefficient of thermal conductivity of solid camphor.

The comparison between the theoretical and experimental ablation rates at the nose are given in the table on page 24.

Note that the theoretical values for the stagnation point ablation rate are greater than the experimental values in all cases. One principal error in the theoretical results could be the existence of non-equilibrium conditions at the surface. For example convection in the boundary layer flow may cause the vapor concentration next to the wall to be less than the equilibrium value; this would cause the B' value to decrease for constant T_o (See Eq. (3).), and hence the constant pressure lines in Figures 1 through 3 would be shifted to the right. If this should happen, T_W would rise, and $\dot{q}_w$ and $\dot{m}$ would decrease. Hence this result could in part explain the fact that the experimental ablation rates at the nose

	Reservoir Pressure (atm.)	Ablation Rate at the Nose (cm./min.)		
		Experiment	Theory ($\dot{q}_s=0$)	Theory ($\dot{q}_s \neq 0$)
$M_\infty = 5.8$				
H_2O-ice	2.00	0.047	0.081	.075
$C_{10}H_{16}O$-ice	2.34	0.173	0.350	.340
$C_{10}H_{16}O$-ice	3.70	0.200	0.391	.380
$M_\infty = 8.0$				
H_2O-ice	3.70	0.128	0.168	.161
$C_{10}H_{16}O$-ice	5.06	0.630	0.944	.943

are less than the theoretical values. Conversely, if the vapor concentration next to the wall is higher than the equilibrium value, then the wall temperature will decrease.

If the experimental temperature data are qualitatively correct on the model afterbody, then Figures 21 and 23 indicate that K_E was less than equilibrium on the afterbody for H_2O-ice and greater than equilibrium on the afterbody for $C_{10}H_{16}O$-ice.

Conduction of heat into the interior of the body (positive $\dot{q}_s$) would cause B' to decrease for fixed T_W (See Eq. (2).) and hence would cause the constant reservoir temperature lines to shift down in Figures 1 through 3. This would cause the equilibrium T_W to decrease, but only very slightly since the vapor pressure curves are very steep. In any case, as seen by Eq. (8) et. seq.,

$$\dot{m} L_E = \dot{q}_w - \dot{q}_s \quad .$$

Hence, positive $\dot{q}_s$ would effect a reduction in the local ablation rate.

An additional error incurred in the theoretical calculations is that in general Le, Pr, and Sc are not equal to 1.

Factors contributing to the reliability of the theoretical results for $\dot{m}$ are as follows:

(1) If $(T_o - T_w)$ is large then $\dot{q}_s$ becomes relatively less important with respect to $\dot{q}_w$. This result is seen in the table on page 24 where the theoretical predictions for ablation rate in leg 2 are much better than those in leg 1.

(2) If K_E at the wall is small, then the approximation that ρ is constant across the boundary layer is more valid. Here it is seen in the table on page 24 that the theoretical ablation rates for H_2O-ice are better than those for $C_{10}H_{16}O$-ice. Also if K_E is small, any errors incurred in computing C_H/C_{H_O} are reduced commensurately.

(3) The blowing correction C_H/C_{H_O} is based on a correlation of theoretical and experimental results for materials with W_E less than 44. Hence the extrapolation of these results to materials with high molecular weight such as camphor (molecular weight 152.23) is questionable.

Because the vapor in the nose region could be convected around the shoulder of the body before it has sufficient time to diffuse through the boundary layer, and also because p_e and T_w decrease along the surface, the vapor pressure on the afterbody may be greater than the thermodynamic equilibrium value. In this case resolidification which is by definition characteristic of an equilibrium process may become pronounced enough to alter the ablation results appreciably, giving lower values of $\dot{m}$

beyond the shoulder than would be otherwise experienced. Examination of the model film data and telescopic observations indicate that resolidification did occur, but no pronounced effects on the ablation results are apparent. (See Figures 26 through 31.) Resolidification also has the effect of increasing the model roughness, (See particularly Figure 12 near the shoulder.) and hence C_f or C_H with a proportional increase in $\dot{q}_w$; the magnitude of this effect is not known. However, the model roughness observed was on a very small scale incapable of tripping the boundary layer, and nowhere in the data is there a sharp increase in heat transfer rate such as would have been experienced if boundary layer transition to turbulent flow had occurred.

As seen by the photographs of the equilibrium-shape models (Figures 12 and 13) the nose shapes remain convex. This result has important ramifications in that if one is to measure experimentally the ablation rate of a particular body shape it is important that the ablation data be obtained before the body shape is appreciably altered. Ideally, the body shape at the start of each test should duplicate the equilibrium body shape. For the equilibrium body shape obtained experimentally in these tests for $C_{10}H_{16}O$-ice, the axial ablation velocity increases by less than 4 per cent from the stagnation point to the shoulder. (See Figure 32.) The shoulder is taken to be the point where the body slope is 45° to the flow direction.

The pressure distribution for the equilibrium-shape model is similar to the distribution for the hemisphere-cylinder and agrees well with the modified Newtonian prediction out to $\theta = 60^\circ$.

One point in the accuracy of the experimental technique used in this report to obtain ablation rates is worth noting. In using a photographic time-lapse process, absolute errors such as operator prejudice in film reading, distortion of the photographic image, and light refraction by the tunnel window, are less important because errors of this type tend to cancel out when comparing measurements on two frames of film.

V. CONCLUSIONS

The simple theory developed based on an energy balance at the gas-solid interface and using a heat-transfer parameter suggested by other researchers, gives good results for wall temperature, but overestimates the ablation rate by as much as a factor of two. However, the results for the ablation rates are greatly improved for the greater values of $(T_o - T_w)$ and the lower K_E at the wall. The theory may find particular application for estimating the relative merits of different materials. Radiation between the gas and the body, combustion of the ablating materials, and recombination of chemical species at the surface can be accounted for by simple additive terms to the basic heat transfer equation developed in this report. Also for more detailed analyses, more complete account could be taken of the heat conduction into the solid by constructing figures based on Eqs. (2) and (3), but not taking $\dot{q}_s = 0$. However, this effect is second order and is small compared to the simple additive term for $\dot{q}_s$ used in this report.

More research is clearly indicated to determine the magnitude of the shielding effect from blowing by heavy molecules.

The H_2O-ice and camphor models tested in leg 1 for long periods of time attained equilibrium nose shapes in a sense that the changes of shape with time were imperceptibly small. They were close to oblate ellipsoids with a ratio of the major to the minor axis of 1.7 for camphor and 6 for H_2O-ice. An attempt has been made to predict theoretically the axis-ratio by assuming a family of ellipsoids for the equilibrium nose shape, but the results were not satisfactory. It appears that one needs more accurate relations between the body shape and the flow properties outside the boundary layer than those assumed in the analysis.

Transient effects within the ablating material represents an interesting and challenging area for investigation. In this region, one could measure the early timewise ablation rate and temperature distribution within the solid taking care to regulate the initial model temperature. Also there is room for useful research investigating the boundary layer, measuring concentration, temperature, and velocity profiles near ablating bodies. The heat transfer to the wall obtained from boundary layer measurements could be correlated with photographic ablation data and heat transfer measurements within the solid.

REFERENCES

1. Cheng, Sin-I.: Meteoric Ablation through Interfacial Instability. ARS Journal, Vol. 29, No. 8, pp. 579-587, August, 1959.

2. Lees, L.: Ablation in Hypersonic Flows. Paper presented at the 7th Anglo-American Conference, sponsored jointly by the Royal Aeronautical Society and the Institute of the Aeronautical Sciences, New York, N. Y., October 5-7, 1959.

3. Adams, M. C.: Recent Advances in Ablation. ARS Journal, Vol. 29, No. 9, pp. 625-632, September, 1959.

4. Lees, L.: Recovery Dynamics -- Heat Transfer at Hypersonic Speeds in a Planetary Atmosphere. Chapter 12, Space Technology, pp. 12-01 to 12-20, John Wiley and Sons, New York, N. Y., 1959.

5. Lees, L.: Convective Heat Transfer with Mass Addition and Chemical Reactions. Proceedings of the Third Combustion and Propulsion Colloquium, Advisory Group for Aeronautical Research and Development, NATO, Palermo, Sicily, Italy, March 17-21, 1958, pp. 451-498, Pergamon Press, 1958.

6. Kubota, T.: Study of Ablation with Ice Model at M = 5.8. Paper presented at the ARS Semi-Annual Meeting, San Diego, California, June, 1959.

7. Bethe, H. A. and M. C. Adams: A Theory for the Ablation of Glassy Materials. J. of the Aero/Space Sci., Vol. 26, No. 6, pp. 321-328, June, 1959.

8. Fay, J. A. and F. R. Riddell: Theory of Stagnation Point Heat Transfer in Dissociated Air. J. of the Aero. Sci., Vol. 25, No. 2, pp. 73-85, February, 1958.

9. Roberts, L.: Stagnation-Point Shielding by Melting and Vaporization. NASA Report No. 10, April, 1959.

10. Cohen, C. B. and E. Reshotko: The Compressible Laminar Boundary Layer with Heat Transfer and Arbitrary Pressure Gradient. NACA Technical Note 3326, April, 1955.

11. Gazley, C.; D. J. Masson; J. F. Gross: General Characteristics of Binary Boundary Layers with Applications to Sublimation Cooling. Third Symposium on High Speed Aerodynamics and Structures, San Diego, California, Vol. 1, pp. 301-347, March 25-27, 1958.

12. Brooke, E. C.: Heat Transfer to Dry Ice Spheres Subjected to Supersonic Airflow. NAVORD Report 5719, September 1, 1957.

13. Kemp, N. H.; P. H. Rose; R. W. Detra: Laminar Heat Transfer around Blunt Bodies in Dissociated Air. Journal of the Aero/Space Sciences, Vol. 26, No. 7, pp. 431-430, July, 1959.

14. Chones, A. J.: Heat-Transfer and pressure Measurements on Flat-Faced Flared-Tail Circular Cylinders and Normal Discs. NAVORD Report 6669, June 15, 1959.

15. Handbook of Chemistry and Physics, 39th Edition, C. D. Hodgman Editor, Cleveland Chemical Rubber Publishing Company, March, 1958.

16. Weiss, R.: Sublimation of a Hemisphere in Supersonic Flow. Massachusetts Institute of Technology, Naval Supersonic Laboratory, Technical Report 391, July, 1959.

17. International Critical Tables of Numerical Data — Physics, Chemistry and Technology. National Research Council, New York, Mc-Graw-Hill, Inc., 1926, 7 volumes.

18. Reshotko, E.: Simplified Method for Estimating Compressible Laminar Heat Transfer with Pressure Gradient. NACA Technical Note 3888, December, 1956.

19. Vinokur, M.: Inviscid Hypersonic Flow Around Blunt Bodies. Lockheed Aircraft Corporation, LMSD-48454, 16 March 1959.

APPENDIX A

PROPERTIES OF MATERIALS

Material	Water	Camphor
Chemical Formula	H_2O	$C_{10}H_{16}O$
Molecular Weight (W_E)	18.02	153.23
Conductivity (k) (cal./cm. sec. °C)	0.002 - 0.005*	4.81×10^{-4} **
Density (ρ) (gms./cm.^{3})	0.917 ***	0.953 experimentally determined
Latent Heat of Sublimation (L_V) (cal./gm.)	676 ****	84.1 *****
Diffusion Coefficient of Vapor in Air (D_{12}) (cm.^{2}/sec.)	0.220 ******	0.045 $\pm$ 0.015 estimated
Viscosity of Vapor at 0°C ( ) (poise . 10^6)	88 *******	--

---

* Reference 15, page 2256.

** Reference 16, page 30.

*** Reference 15, page 1985.

**** op. cit., pages 2134, 2138.

***** op. cit., page 2248.

****** Reference 17, Vol. 5, page 62.

******* op. cit., page 4.

Structural formula for camphor:

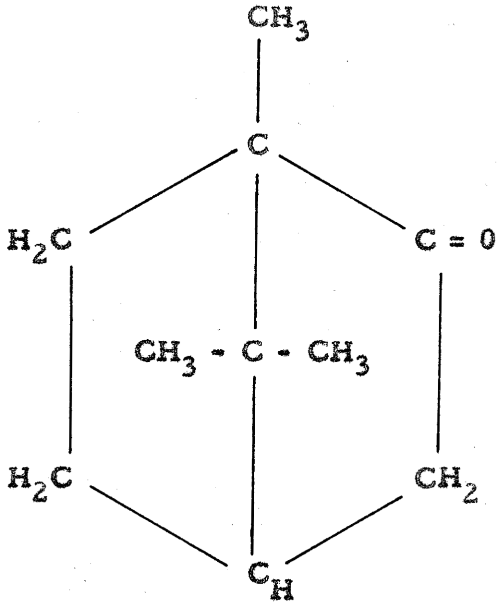

APPENDIX B

ILLUSTRATION OF THE COMPUTATIONAL TECHNIQUE

Consider a blunt-nosed axially symmetric body in an airstream of Mach number M_∞ with a bow shock and boundary layer behind the shock covering the body as in the following sketch.

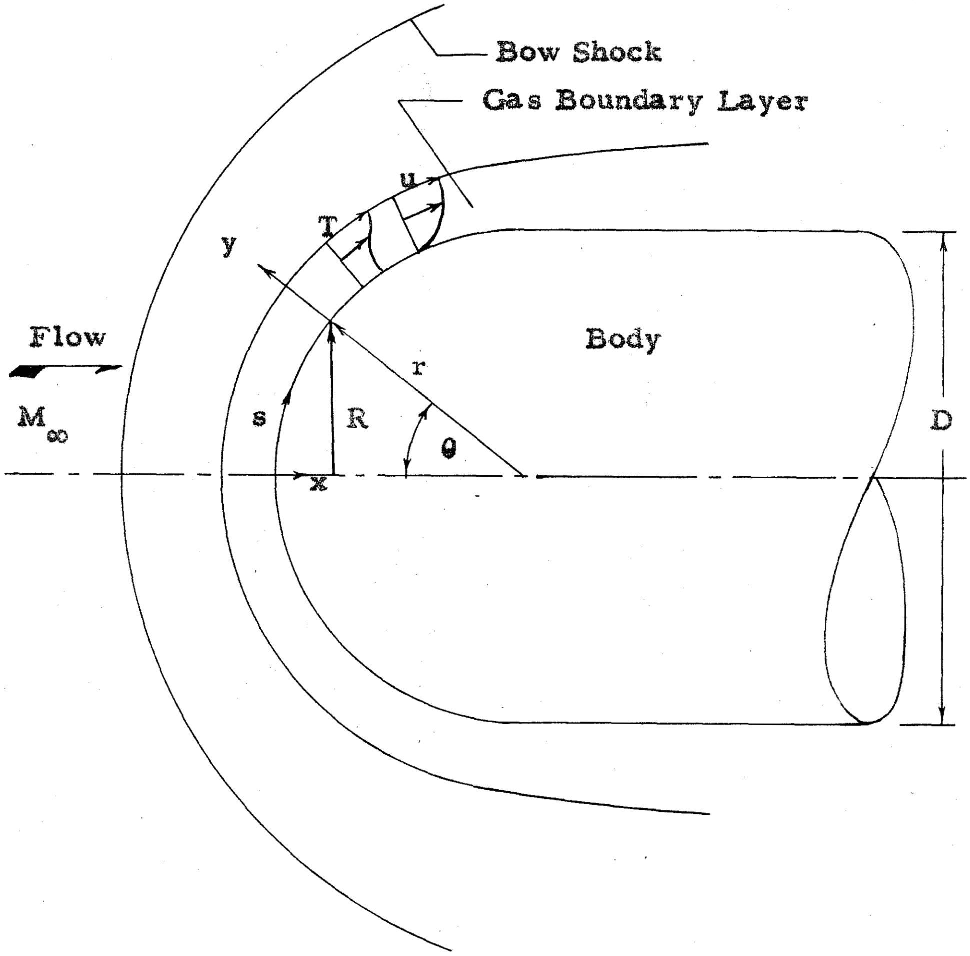

Eq. (9) was used to solve for the heat transfer rate to the wall along the body surface. The values for the heat transfer parameter $(Nu/\sqrt{Re_s})_w$ were computed by a procedure worked out by Cohen[10] and Reshotko as outlined below.

The pressure ratio p_e/p_o' was computed by the modified Newtonian distribution

$$p_e/p_o' = \cos^2 \theta + (p_\infty/p_o') \sin^2 \theta$$

up to values of θ at which the slope of the Newtonian pressure distribution, $d(p_e/p_o')/d\theta$, was equal to the magnitude and slope obtained by the Prandtl-Meyer function. The pressure was then assumed to follow a Prandtl-Meyer distribution out to $\theta = 70^\circ$ from where the data were faired into the experimental values. Experimental values of p_e/p_o' were measured on a 3/4 scale model at $\theta = 0^\circ, 45^\circ, 90^\circ$, and at various stations along the body. The modified Newtonian distribution was found to give excellent agreement with experiment at $\theta = 45^\circ$. Once the pressure distribution was determined, Mach number and T_e/T_o were determined analytically from p_e/p_o', and T_w was determined directly from the charts of B' versus T_w. Then as suggested in Reference 10, a correlation number, n, was determined by numerically integrating the equation

$$\frac{n}{P'(T_o/T_e)} = 0.44\,(T_e/T_o)^{-4}\,\frac{M_e^{1-A}}{R^2}\int_o^{s/D} (T_e/T_o)^4\,\frac{R^2}{M_e^{1-A}}\,d\,(s/D)$$

where

$$P' = \frac{d(p_e/p_o')/d(s/D)}{(p_e/p_o')\,M_e^2}$$

$$A = -\left(\frac{0.44}{n_{s.p.}} + 2\right) .$$

The Reynolds analogy parameter, $\left(\frac{\ell}{\frac{C_f\, Re_s}{Nu}} \right)_{Pr=1}$,

was obtained from Figure 2, page 13, in Reference 18, versus n and T_w/T_o. Then,

$$\left(\frac{Nu}{\sqrt{Re_s}} \right)_w = 2\, Pr^{\alpha} \sqrt{\frac{s/D}{n/(P' \frac{T_o}{T_e})}} \left(\frac{\ell}{\frac{C_f\, Re_s}{Nu}} \right)_{Pr=1}$$

where α was taken as 1/3.

Values of μ_w were determined from Sutherland's formula and ρ_w was determined from the equation of state for a perfect gas both values are for air at the wall temperature.

Once $(Nu/(Pr\ \sqrt{Re_s})_w$ is determined in this manner it is easy to solve Eq. (9) for $\dot{q}_w$ along the surface.

Pr, c_p , and   were assumed to be constants, 0.70, 0.2404 cal/gm°C, and 1.4, respectively.

This method has the advantage of being straightforward and requiring no iteration. The numerical integration is best done analytically near the stagnation point since the integral (a small number) must be divided by the integrand (a small number). Near the stagnation point one may take

$$n/P'\,(T_o/T_e) \cong (0.44)/(A+2)\,.\,(s/D) \quad .$$

For the calculations with blunt bodies encountered in this report, this linear equation was found to be accurate within 5 per cent out to values of $s/D = 0.2$. Further, B' is such an insensitive function of p_e that it is possible to assume $C_{H_O}/C_H = 1 + \beta B' =$ constant to good accuracy where β is small.

APPENDIX C

CORRECTION FOR CONDUCTION EFFECTS AT THE NOSE

Because of the large temperature difference at the nose and at the shoulder of the models significant errors may be incurred by assuming the heat conducted into the solid interior is negligible. Barring the use of brute force numerical methods it is possible to get an estimate of the magnitude of such errors by means of a simple model. Consider the hemispherical nose of the model to have a temperature distribution on its surface equal to the theoretical equilibrium temperature and a uniform temperature distribution over the base given by the theoretical equilibrium shoulder temperature. Laplace's equation in spherical polar coordinates for an axially symmetric body gives

$$\nabla^2 T = 0 = \frac{1}{r^2}\frac{\partial}{\partial r}\left(r^2 \frac{\partial T}{\partial r}\right) + \frac{1}{r^2 \sin\theta}\frac{\partial}{\partial \theta}\left(\sin\theta \frac{\partial T}{\partial \theta}\right) .$$

Separating variables, $T = R(r)\,\Theta(\theta)$, and applying the boundary condition, $T = 0$ at $\theta = \pm (\pi/2)$,

$$T(r, \theta) = \sum_{n=0}^{\infty} a_n r^{2n+1} P_{2n+1}(\cos\theta)$$

where Pn's are the Legendre's polynomials.

Then set

$$T_w(1, \theta) = \sum_{n=0}^{\infty} a_n P_{2n+1}(\cos\theta) ,$$

where $T_w(1, \theta)$ is known. From this the a_n's are determined.

Differentiate and solve to obtain

$$(\partial T/\partial r)_w(s) = \sum_{n=0}^{\infty} (2n+1)\ a_n\ P_{2n+1}(\cos\theta).$$

Once, $(\partial T/\partial r)_w(s)$ is determined, $\dot{q}_s$ may be determined by

$$\dot{q}_s = k_E\,(\partial T/\partial r)_w(s) \quad .$$

For practical purposes the summation was not made from 0 to infinity. The temperature distribution followed a cosine function so closely that only the Legendre polynomial P_1 was retained. The effect of conduction is to decrease the ablation rate at the nose, the estimates of these effects are shown in Figures 26 through 31.

APPENDIX D

ANALYSIS OF EQUILIBRIUM NOSE SHAPE

Reference 18 gives the approximate relationship for calculating the laminar heat transfer on an arbitrary body

$$\left(Nu/\sqrt{Re_s} \right)_w = (0.22)\ Pr^{\alpha}\ \sqrt{s/D} \left\{ \frac{G}{F(s)} \int_0^{s/D} F(t)\ dt \right\}^{-\frac{1}{2}}$$

where

$$F(s) = (T_e/T_o)^K\ M_e^{B-1}\ R^2$$

$$K = (\gamma + 1)/(\gamma - 1)$$

$$G = \text{a number}$$

R is the local cross-section radius of the body, and

$$\frac{2\ell}{\left(\dfrac{C_f\ Re_w}{Nu} \right)_{Pr=1}}$$

is assumed = 0.22 (the flat plate value). Near the stagnation point one may assume a linear velocity profile, hence

$$u_e = C_1\ a^*\ s \quad .$$

Then from the isentropic flow relations

$$\begin{aligned} T_e/T_o &= 1 - \frac{\gamma - 1}{\gamma + 1} (u_e/a^*)^2 \\ &= 1 - \frac{\gamma - 1}{\gamma + 1} (C_1\ s)^2 \end{aligned}$$

$$\begin{aligned} M_e^2 &= \frac{2}{\gamma + 1} (u_e/a^*)^2 \left[1 - \frac{\gamma - 1}{\gamma + 1} (u_e/a^*)^2 \right]^{-1} \\ &= \frac{2}{\gamma + 1} (C_1\ s)^2 \left[1 - \frac{\gamma - 1}{\gamma + 1} (C_1 s)^2 \right]^{-1} \quad . \end{aligned}$$

Also, near the stagnation point for blunt bodies

$$R = s\left[1 - (1/6)(s/r)^2 + \dots\right], \quad r = \text{radius of curvature at nose.}$$

Hence, substituting for F(x) and F(t) from these relations and simplifying, one obtains near the stagnation point

$$(\mathrm{Nu}/\sqrt{\mathrm{Re}_s})_w = 0.22\ \mathrm{Pr}^a\sqrt{\frac{2B+1}{D}}\left[1 - \frac{1}{2A+3}\left\{(K - A + 1)\frac{\gamma-1}{\gamma+1}C_1^{\,2} + (1/3r^2)\right\} s^2 + \dots\right] .$$

Evaluating this at the stagnation point, the term in square brackets becomes 1, and

$$\frac{(\mathrm{Nu}/\sqrt{\mathrm{Re}_s})_w}{(\mathrm{Nu}/\sqrt{\mathrm{Re}_s})_{s.p.}} = 1 - \frac{1}{2A+3}\left\{\frac{1}{3r^2} - (A-5)\frac{\gamma-1}{\gamma+1}C_1^{\,2}\right\} s^2 + \dots$$

This equation is limited to the region close to the stagnation point. Reference 14 presents experimentally obtained plots of u_e/a^* for flat nosed bodies at Mach numbers between 2.15 and 4.86 and obtains velocity profiles linear within 5 per cent for s/D less than 0.3. For flat nosed bodies $r \longrightarrow \infty$, and hence $1/r^2 = 0$.

(1) At A = 5, the term in brackets in the last equation becomes zero, hence the ratio of the heat transfer coefficient to its stagnation point value is 1, and the nose will remain flat in the region of the stagnation point.

(2) If A > 5, the heat transfer parameter increases away from the stagnation point hence the ablation rate will increase and the nose will become convex.

(3) If A < 5, the heat transfer parameter decreases away from the stagnation point, hence the ablation rate will decrease, and the nose

will tend to become concave.

From Reference 10, Figure 5, the result is obtained that $A < 5$ for $T_w/T_o < 0.8$ and vice versa.

By Eq. (9)

$$(Nu/ \sqrt{Re_s})_w = \frac{\dot{q}_w \ Pr}{\sqrt{\frac{\rho_w \mu_w u_e}{s}} \ C_{p_A} \ (T_o - T_w)} .$$

But the condition for an equilibrium nose shape, if $\dot{q}_s = 0$, is that $\dot{q}_w/\dot{q}_{s.p.} = \cos\theta$, also $(u_e/s) = du_e/ds_{s.p.} = C_1 \ a^*$ for a linear velocity profile, hence

$$\frac{(Nu/ \sqrt{Re_s})_w}{(Nu/ \sqrt{Re_s})_{s.p.}} = \cos\theta = dR/ds$$

$$= 1 - \tfrac{1}{2} (s/r)^2 + 0 \ (s^4/r^4) .$$

Equating this result with the result on the last page,

$$(1/2r^2) = (1/2A+3) \left\{ (1/3r^2) - (A-5) \ (\gamma -1/\gamma+1) \ C_1{}^2 \right\}$$

or

$$\left(\frac{2A+3}{2} - \frac{1}{3} \right) (1/r^2) = (5-A) \ (\gamma-1/\gamma+1) \ C_1{}^2 .$$

But, $C_1 = (1/a^*) \ (du_e/ds)$, hence

$$\left[(r/a^*) \ (du_e/ds) \right]^2 = \frac{6A+7}{6(5-A)} \ \frac{\gamma+1}{\gamma-1} .$$

By determining $(r/a^*)(du_e/ds)$ for a family of ellipsoid-nosed cylinders with ratios of minor to major axes of the ellipsoids between

1 and 0*, one can solve the above relationship for the shape of the ellipsoid that is compatible with the equilibrium nose condition.

The above analysis offers a means of predicting whether an initially flat nose will tend to become convex or concave. If the nose tends to become convex, then one may assume a general type of nose shape such as an ellipsoid and predict an equilibrium shape from that. This only works if one knows the general type of nose shape in advance. For the conditions of the experiment in this report, the ratio of the major axis to the minor axis was overestimated by a factor of 3 for camphor and underestimated by a factor of 0.7 for H_2O-ice.

---

* See Reference 19 for plots of $\left(\frac{a}{u_\infty} \frac{du_e}{ds} \right)_{s.p.}$.

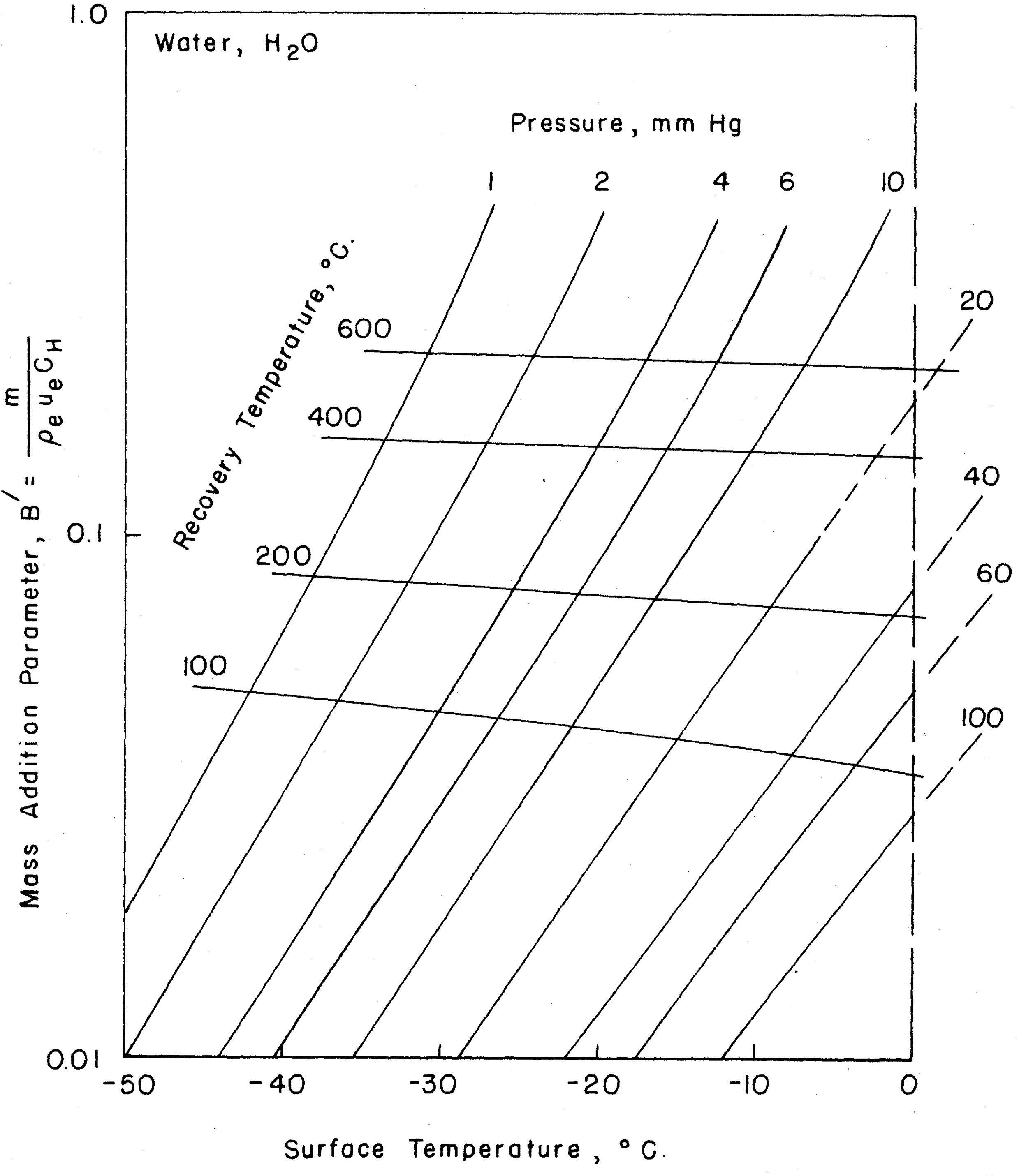

FIG. 1 – MASS ADDITION PARAMETER VS. SURFACE TEMPERATURE

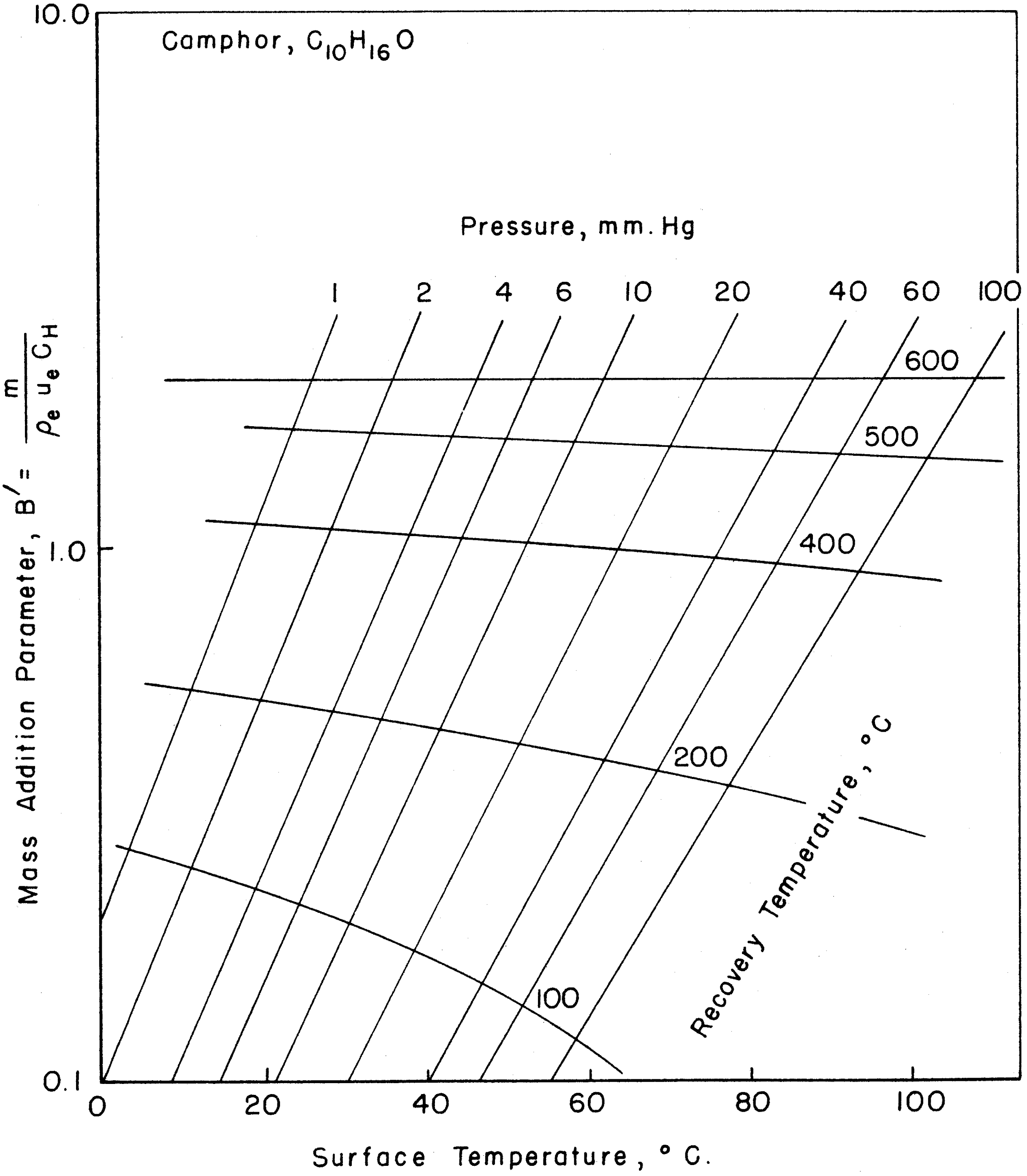

FIG. 2 - MASS ADDITION PARAMETER VS. SURFACE TEMPERATURE

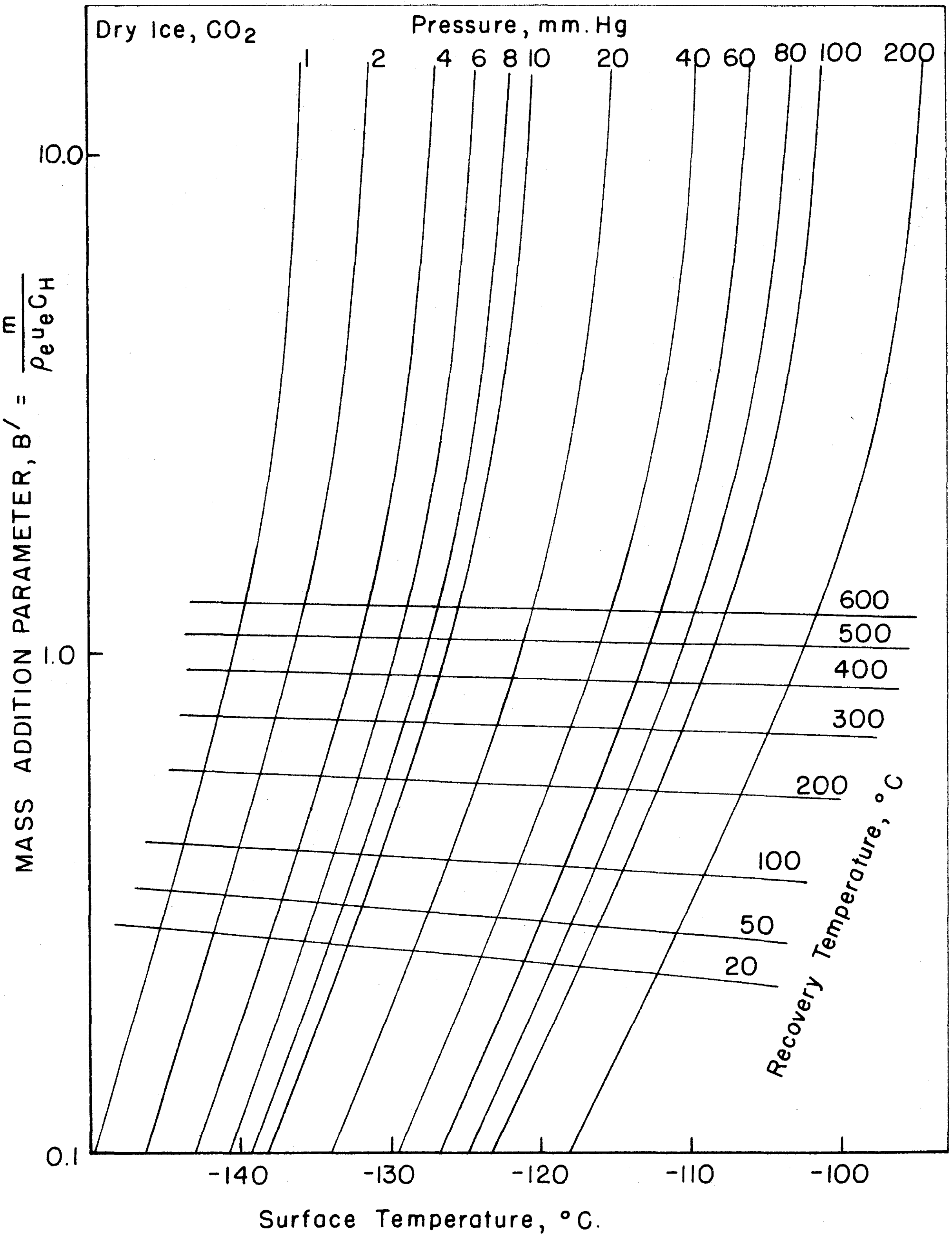

FIG. 3 - MASS ADDITION PARAMETER VS. SURFACE TEMPERATURE

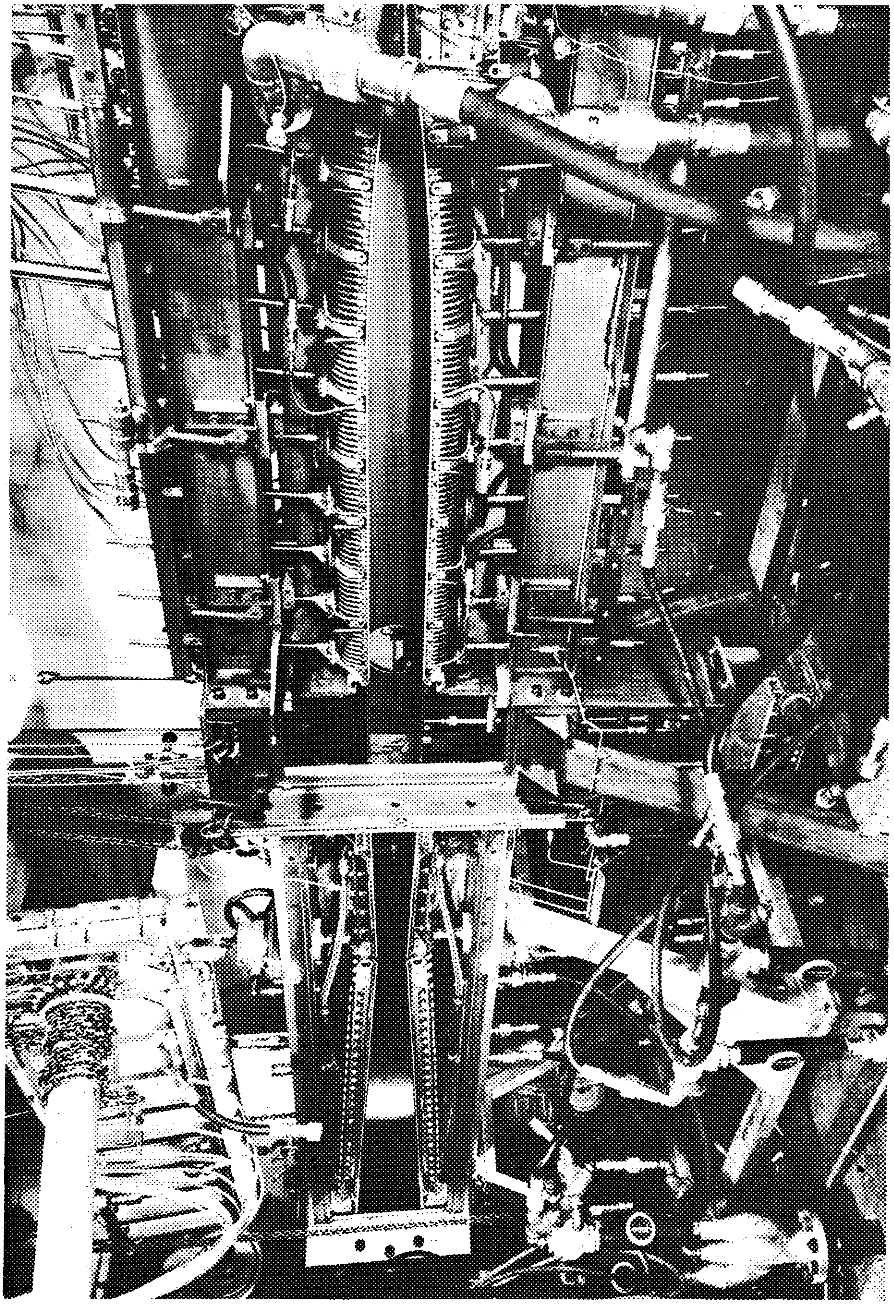

FIG. 4 – THE GALCIT LEG-2 HYPERSONIC TUNNEL

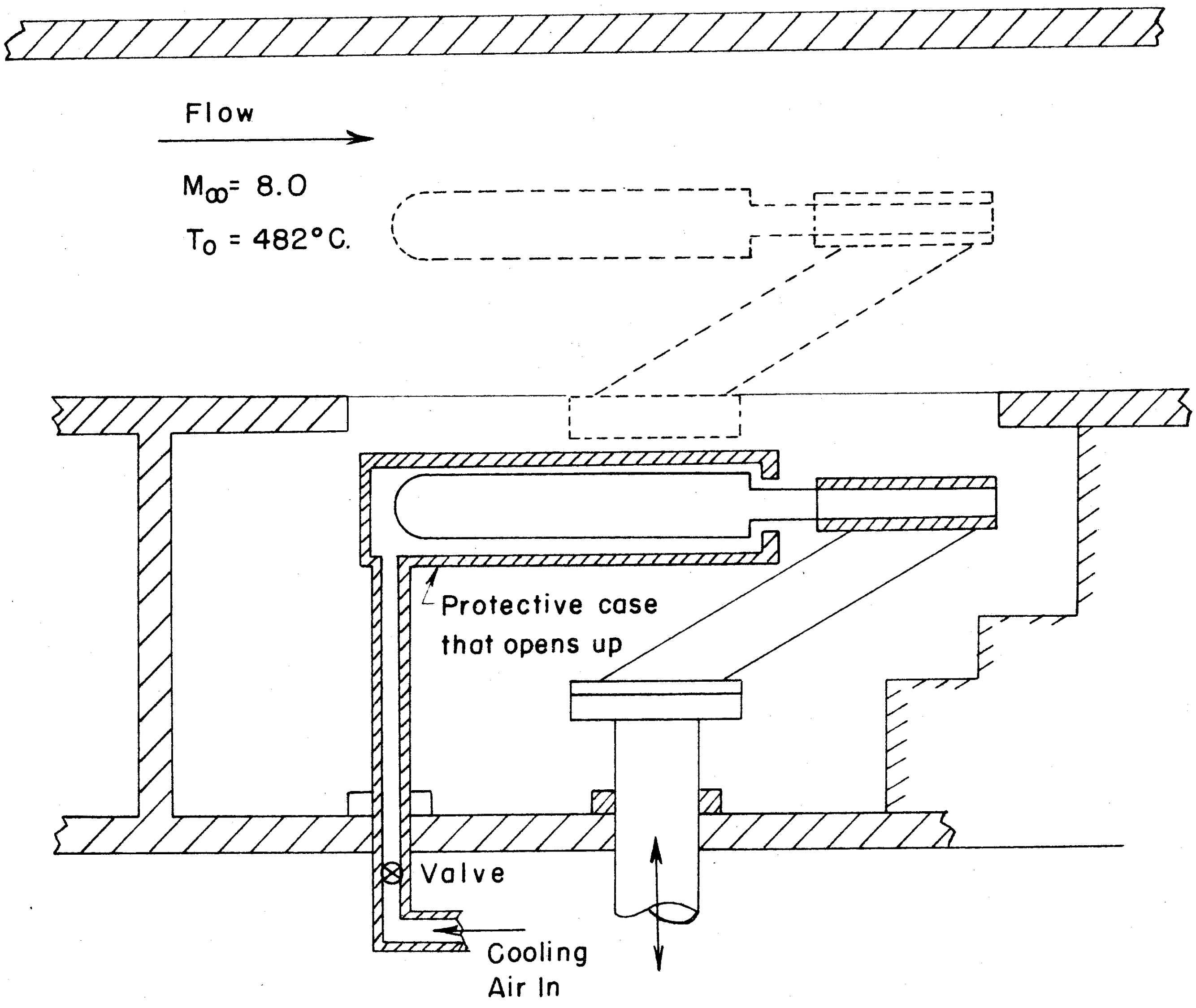

FIG. 5 - LEG 2 MODEL PROTECTOR

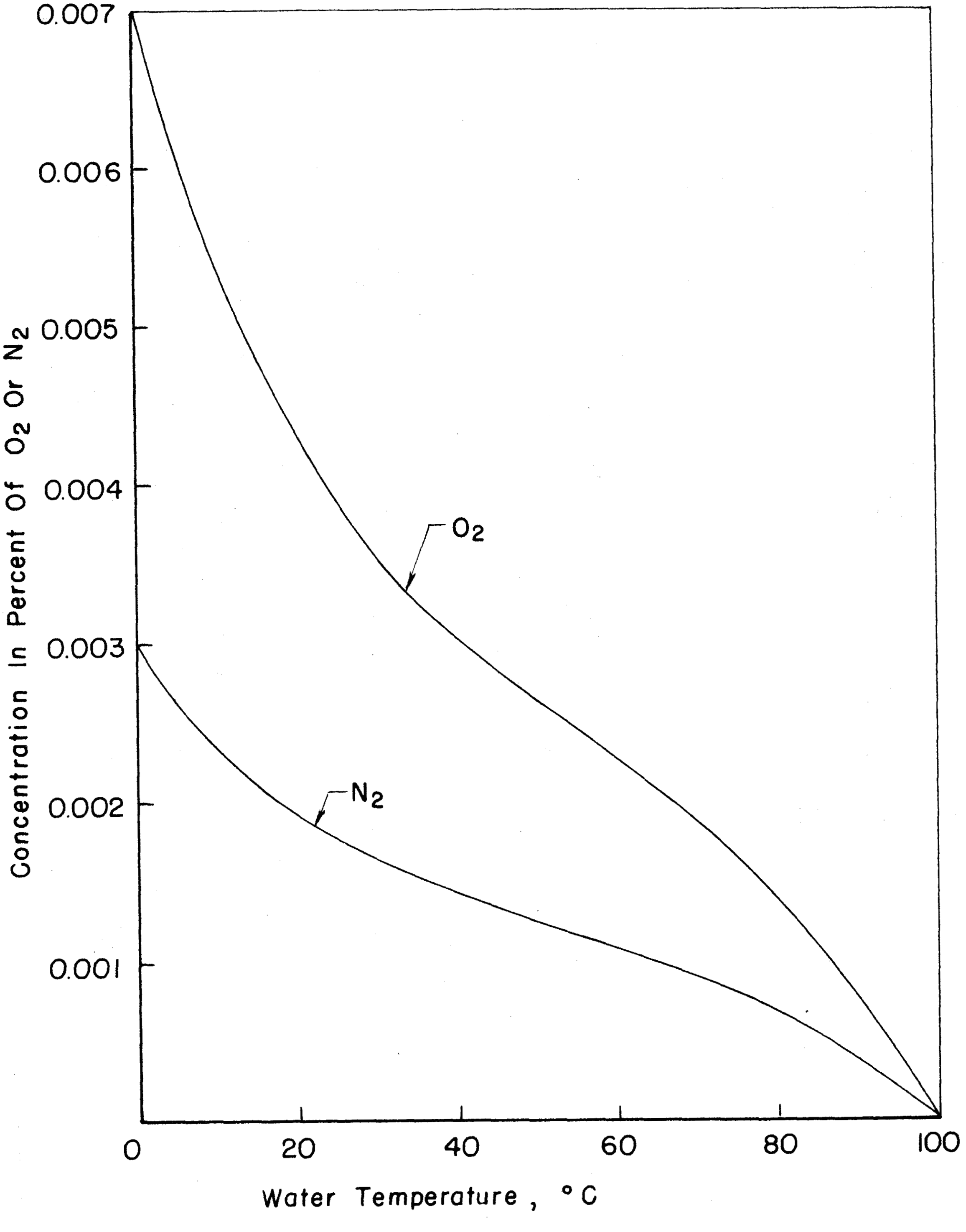

FIG. 6-SOLUBILITY OF O_2 (N_2) IN H_2O WHEN PARTIAL PRESSURE OF GAS PLUS H_2O VAPOR PRESSURE = 1 ATM.

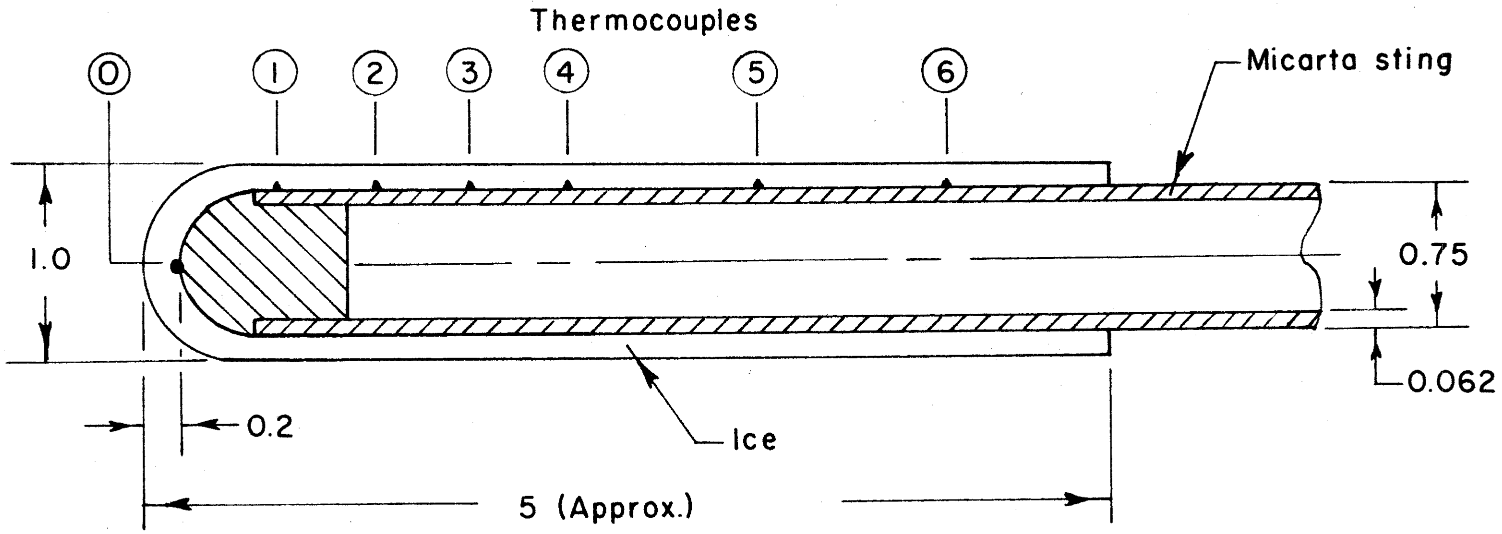

Thermocouple Positions

① 0.7 in. aft of nose
② 1.2 in. " "
③ 1.7 in. " "
④ 2.2 in. " "
⑤ 3.2 in. " "
⑥ 4.2 in. " "

FIG. 7-THERMOCOUPLE MODEL CONSTRUCTION

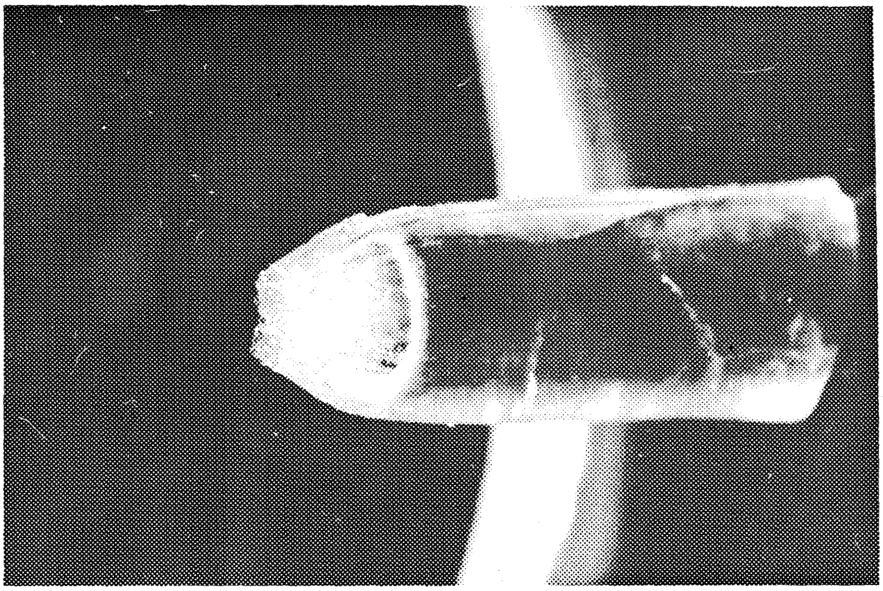

FIG. 8-SEVERE CRATERING OF H_2O-ICE MODEL IN LEG I

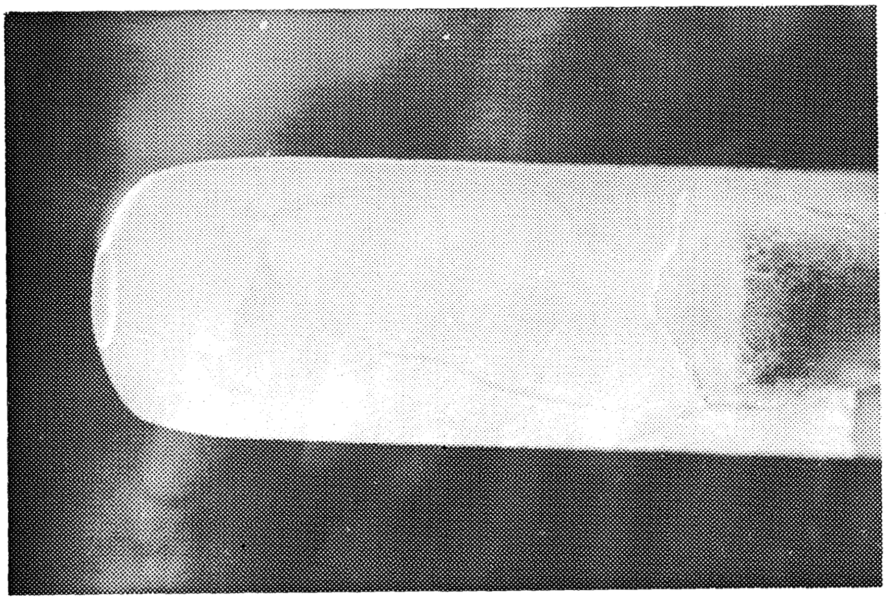

FIG. 9-CONTROLLED CRATERING OF H_2O-ICE MODEL IN LEG I

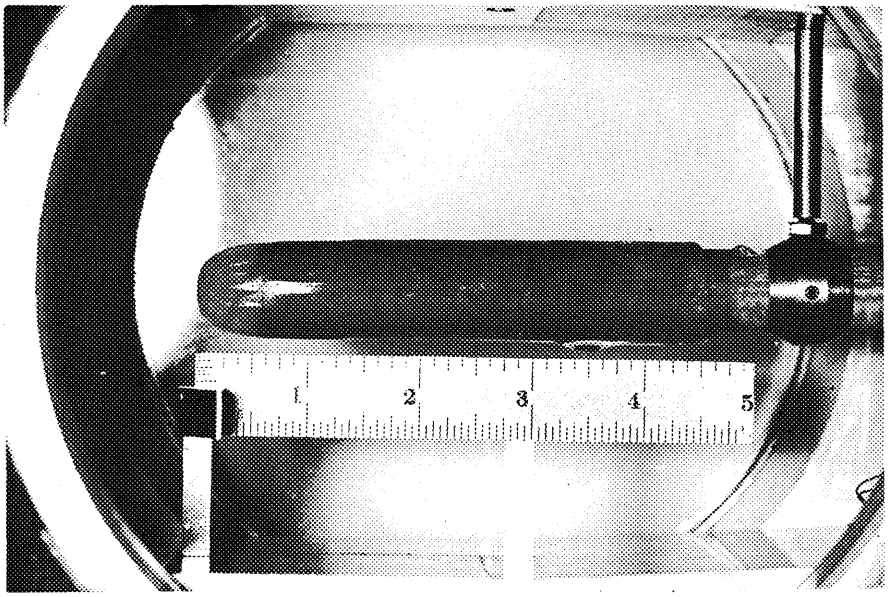

FIG. 10 - H_2O - ICE MODEL IN LEG I AFTER QUANTITATIVE DATA RUN, P_0 = 2.00 ATM.

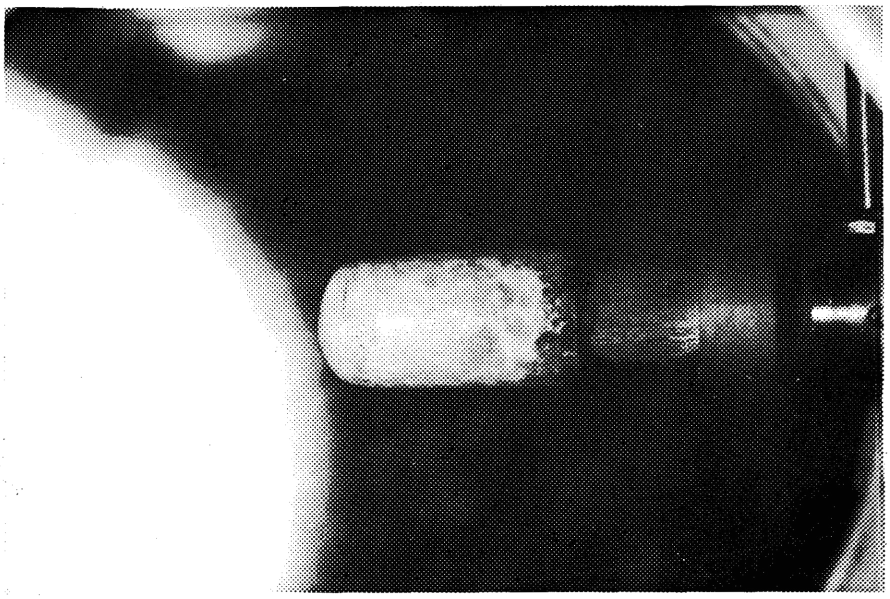

FIG. 11 - $C_{10}H_{16}O$ - ICE MODEL IN LEG I DURING QUANTITATIVE DATA RUN, P_0 = 2.34 ATM.

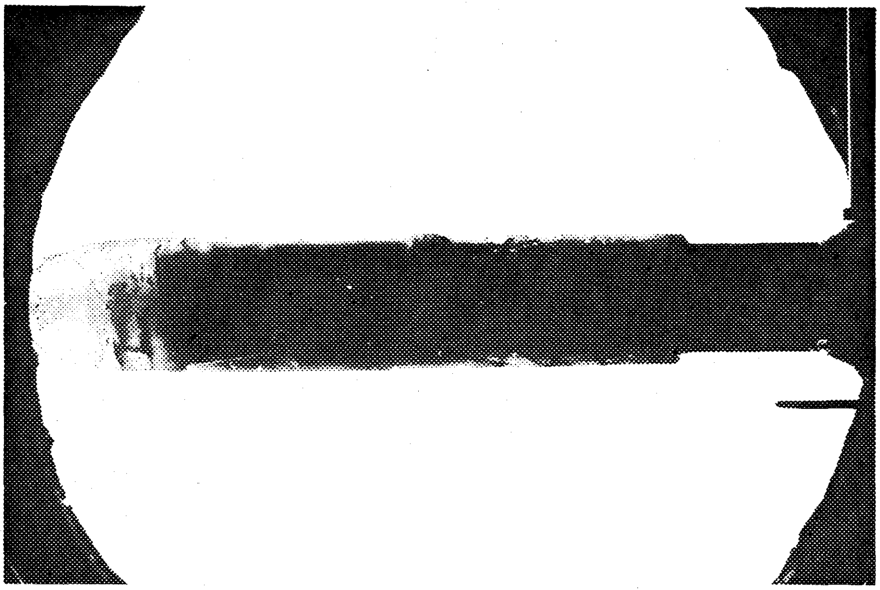

FIG. 12 - EQUILIBRIUM SHAPE FOR H_2O-ICE MODEL IN LEG I, P_o = 2.00 ATM.

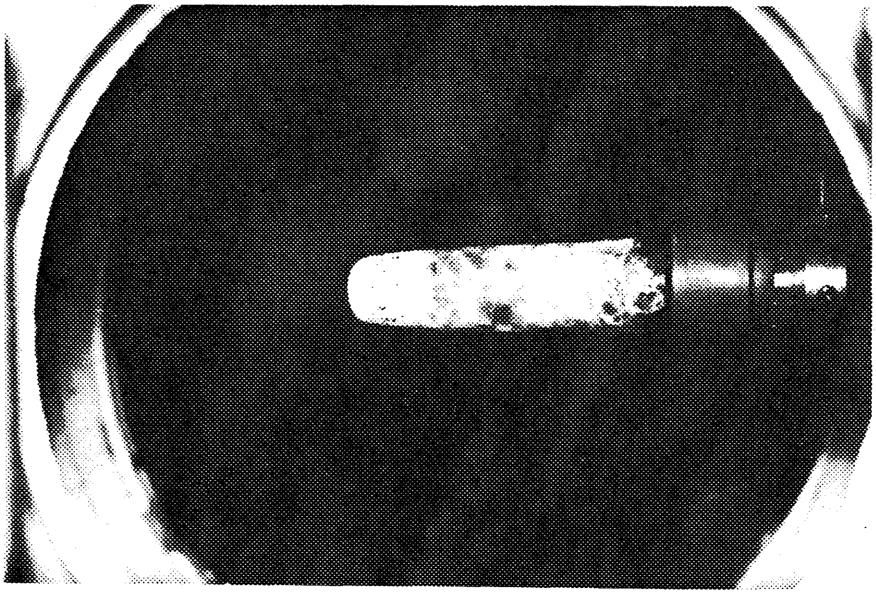

FIG. 13 - EQUILIBRIUM SHAPE FOR $C_{10}H_{16}O$-ICE MODEL IN LEG I, P_o = 2.34 ATM.

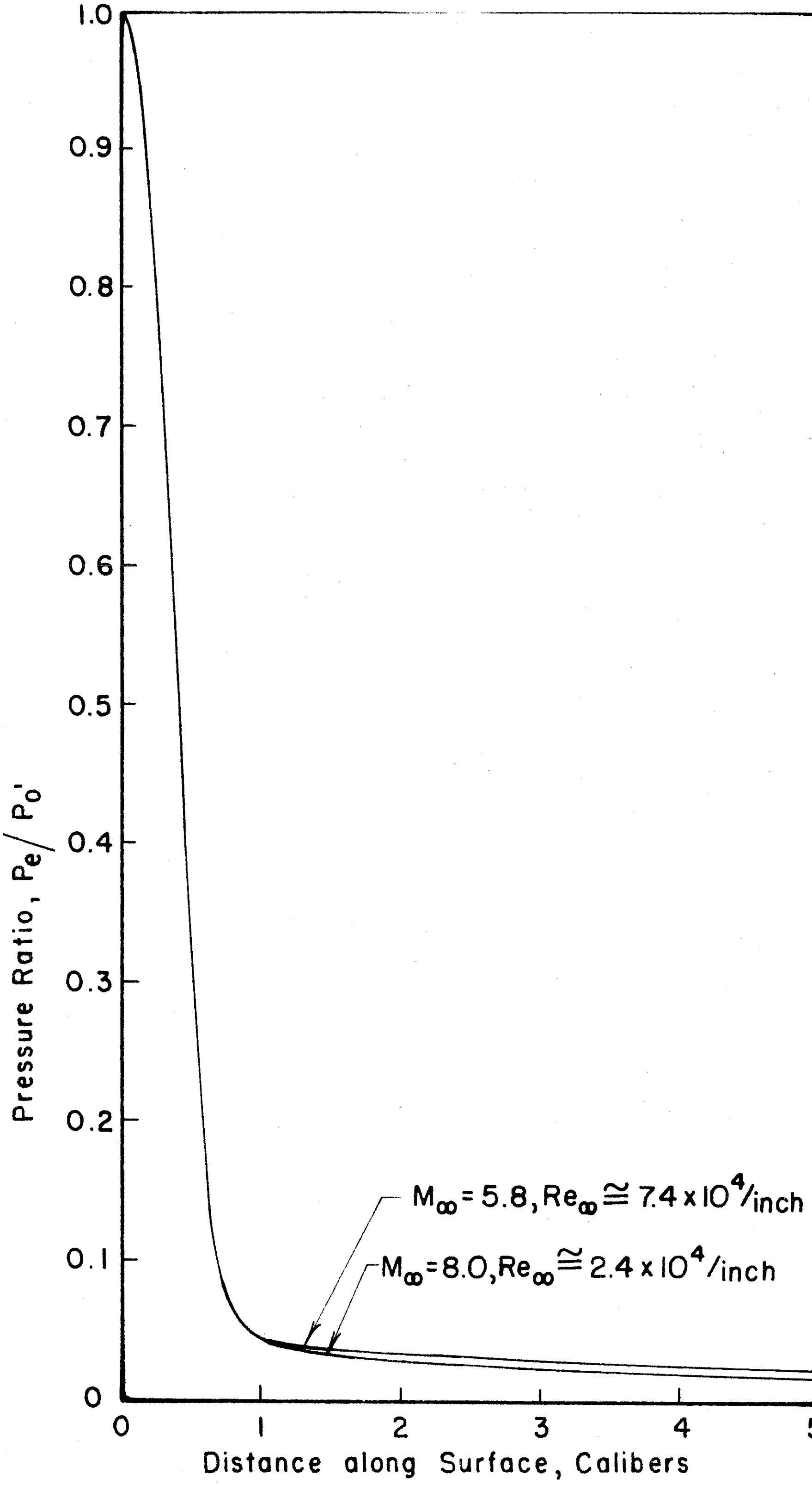

FIG. 14 – PRESSURE DISTRIBUTION ON HEMISPHERE – CYLINDER

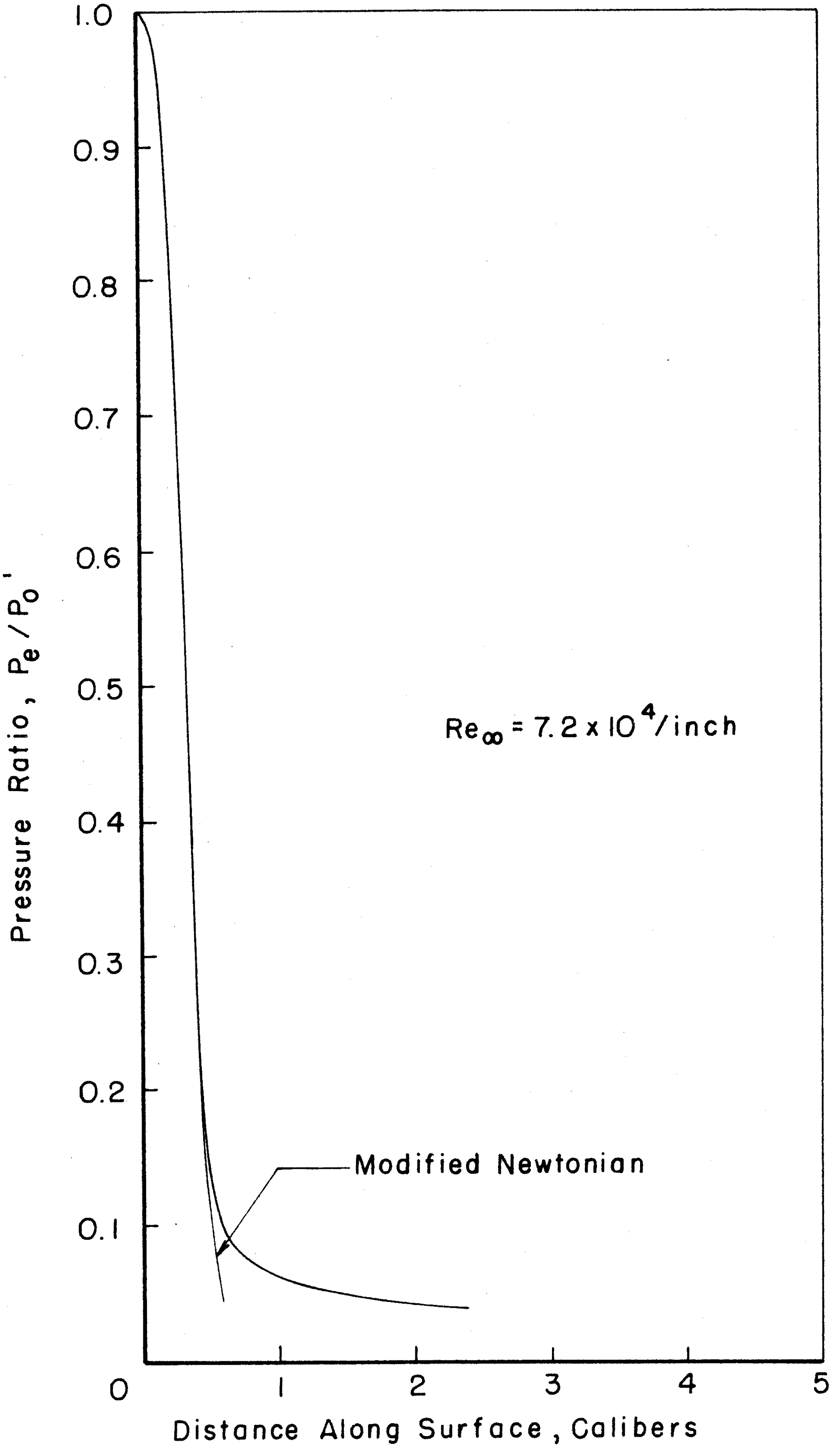

FIG. 15-PRESSURE DISTRIBUTION ON $M_\infty = 5.8$ EQUILIBRIUM-SHAPE PRESSURE MODEL, $C_{10}H_{16}O$-ICE

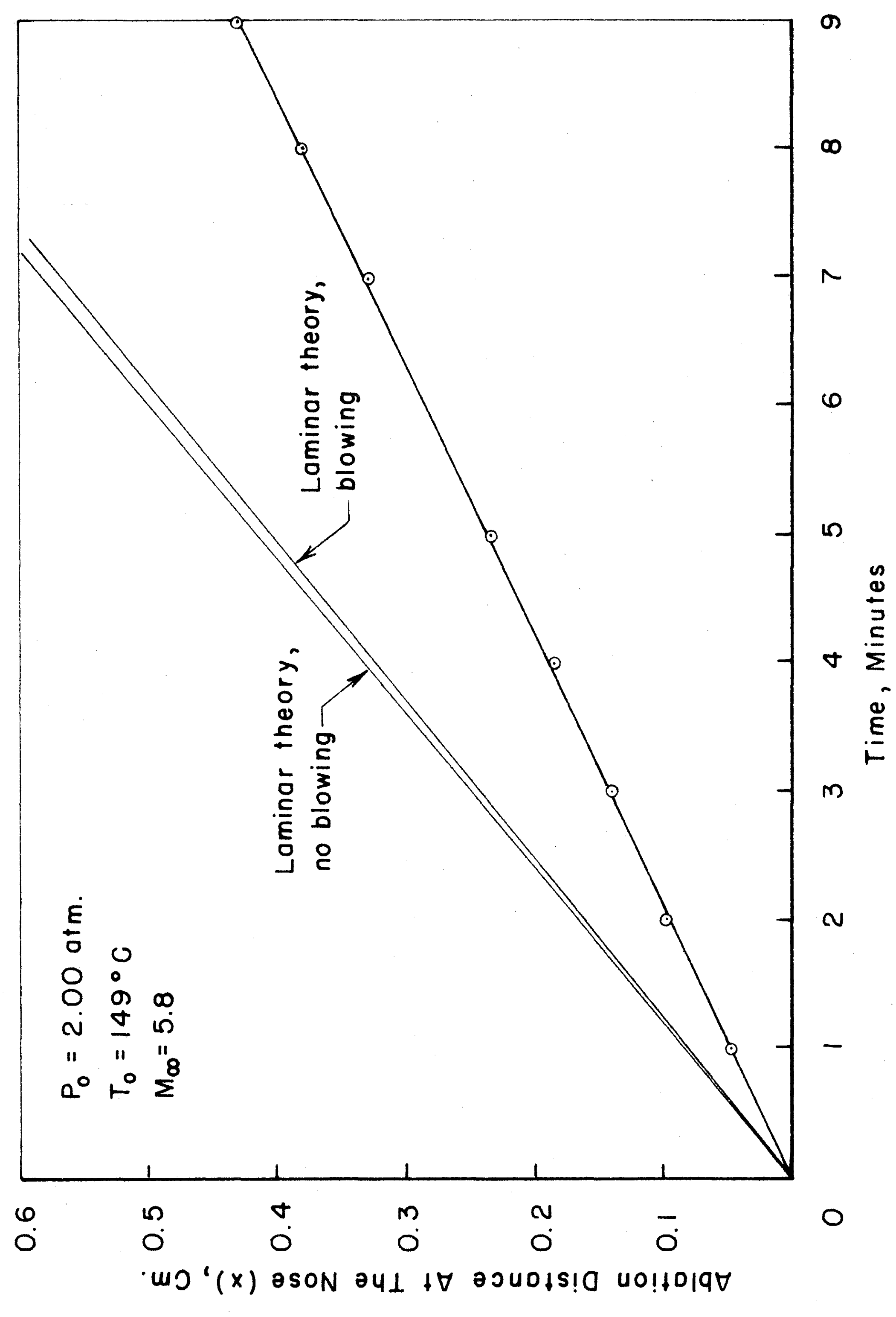

FIG.16-ABLATION RATE AT THE NOSE, H_2O-ICE

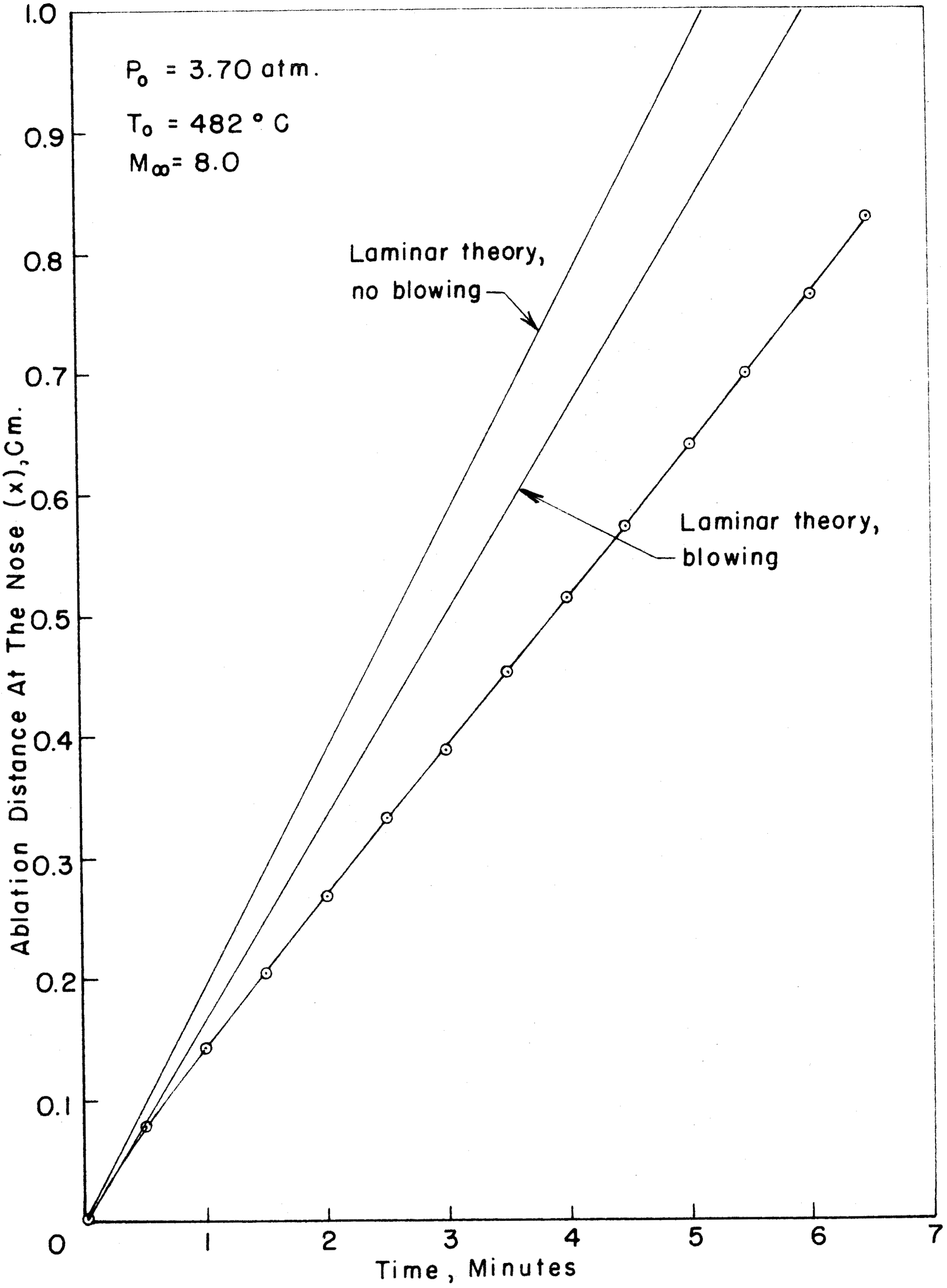

FIG. 17-ABLATION RATE AT THE NOSE, H_2O - ICE

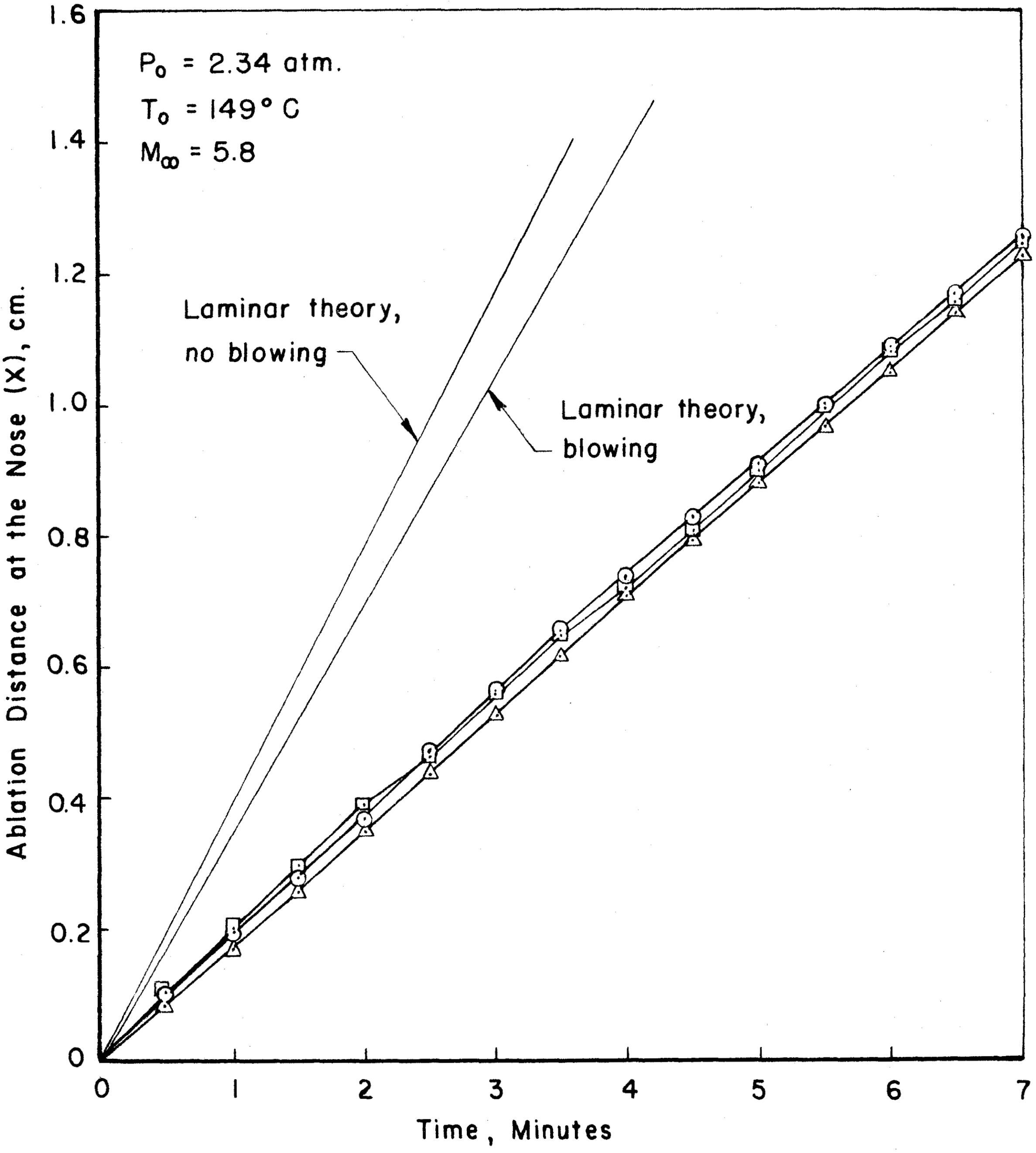

FIG. 18 – ABLATION RATE AT THE NOSE, $C_{10}H_{16}O$ - ICE

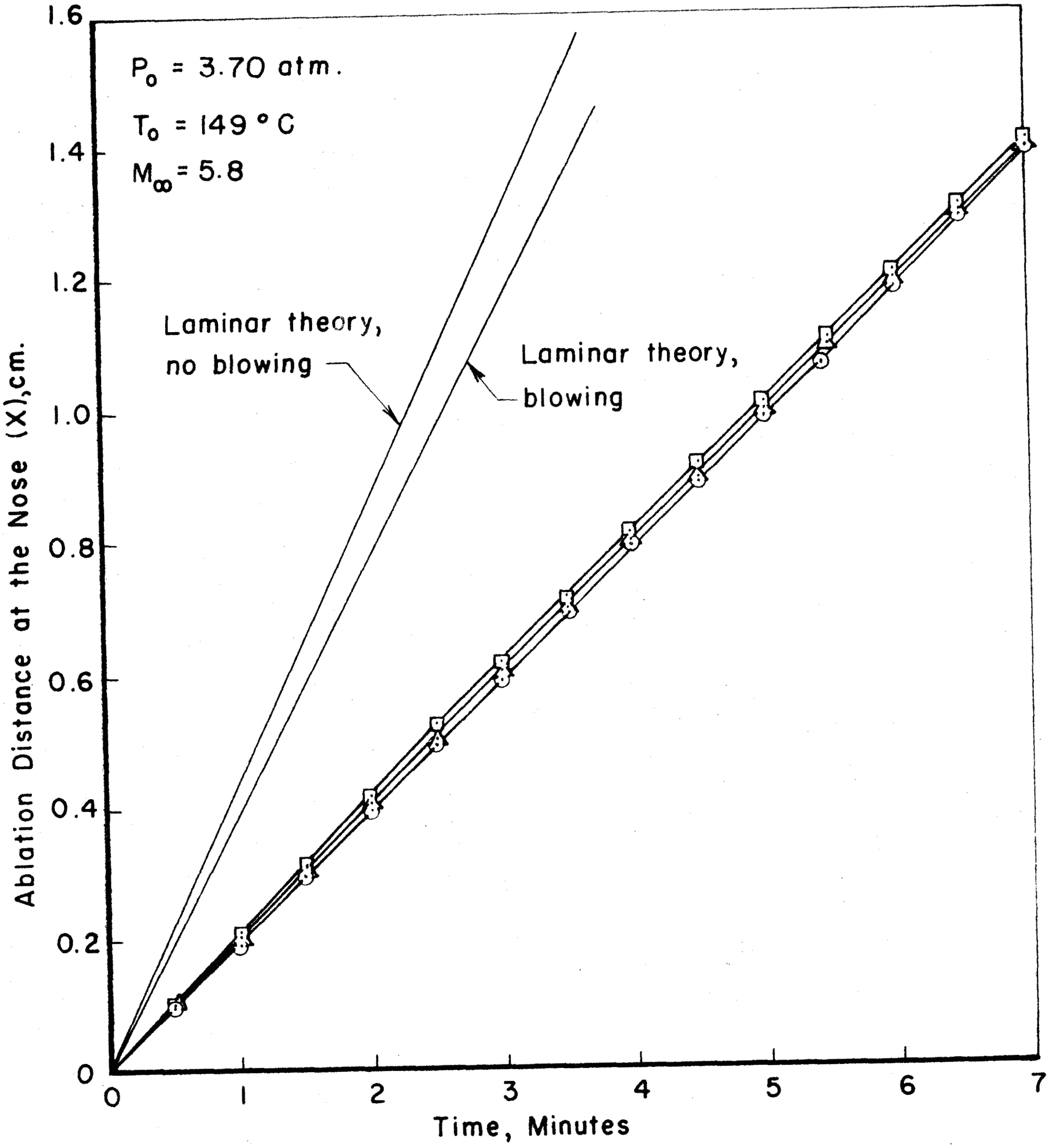

FIG. 19 - ABLATION RATE AT THE NOSE, $C_{10}H_{16}O$ - ICE

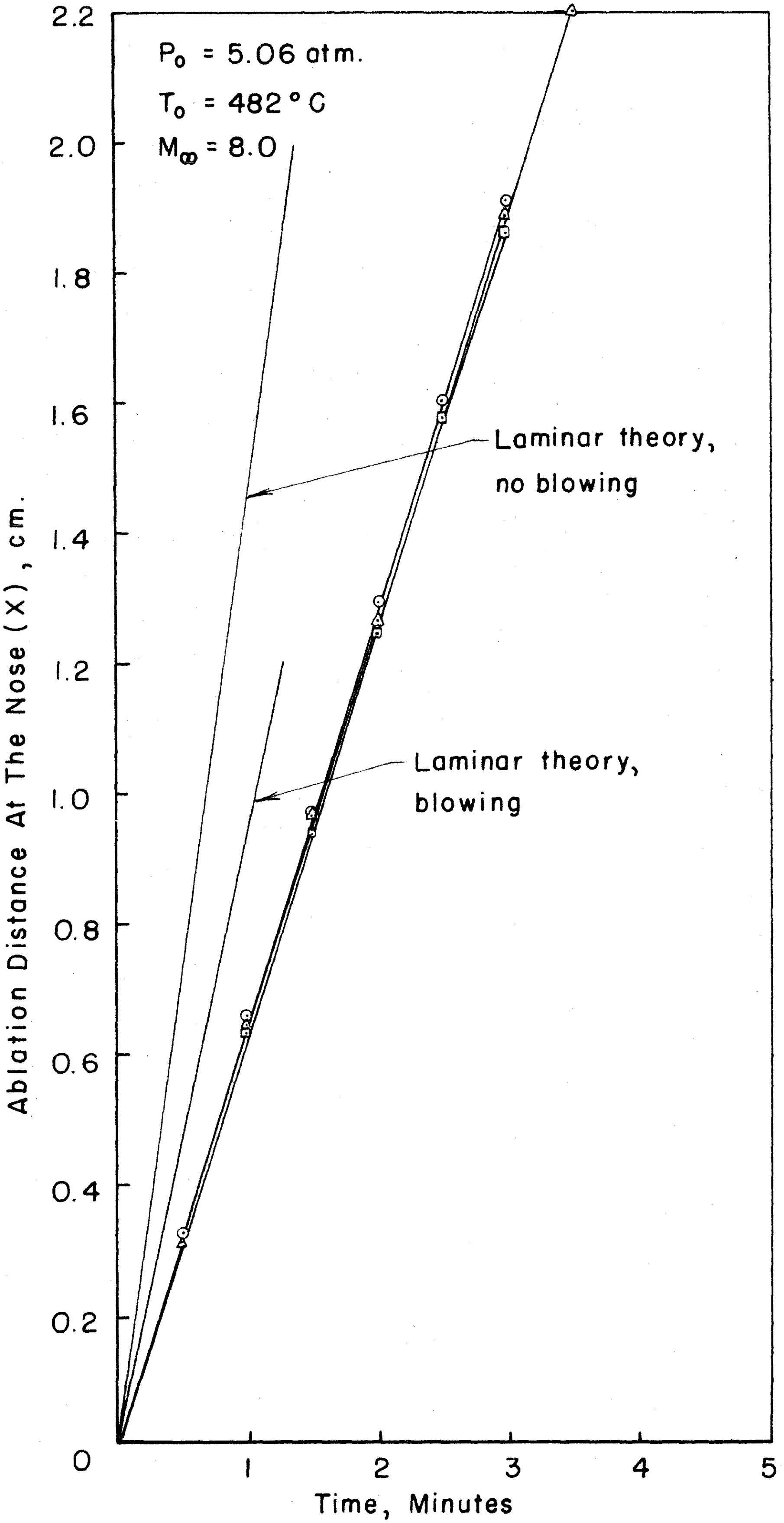

FIG.20-ABLATION RATE AT THE NOSE, $C_{10}H_{16}O$ - ICE

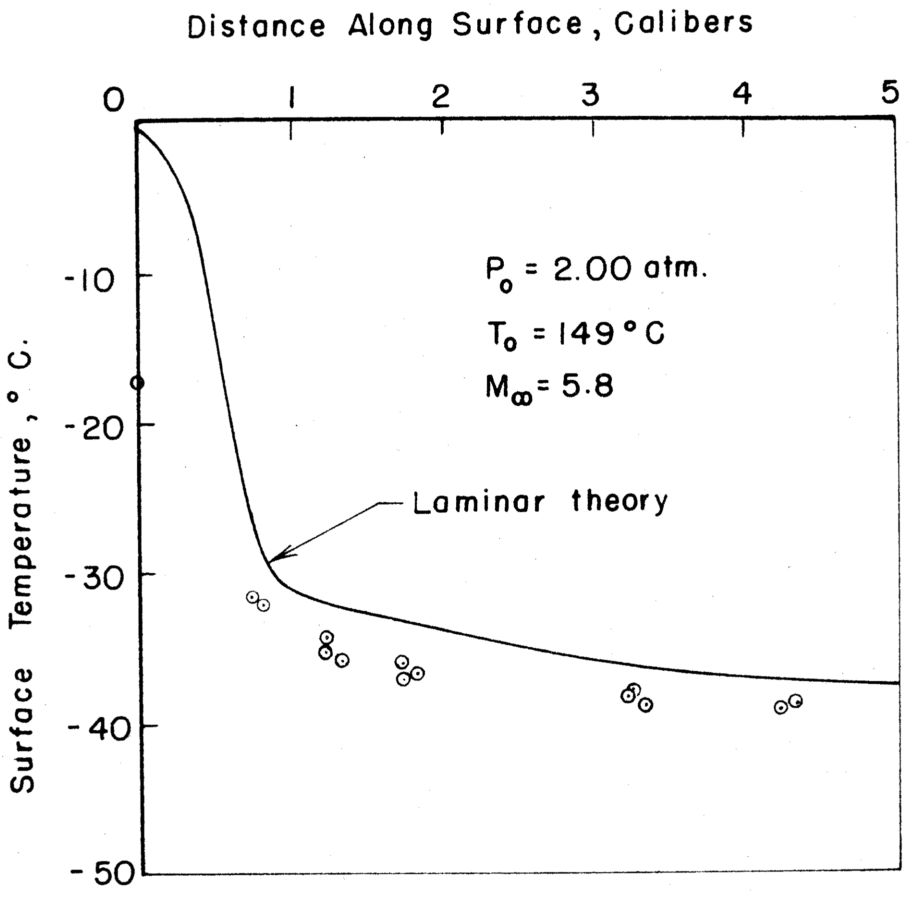

FIG. 21 - SURFACE TEMPERATURE, H_2O - ICE

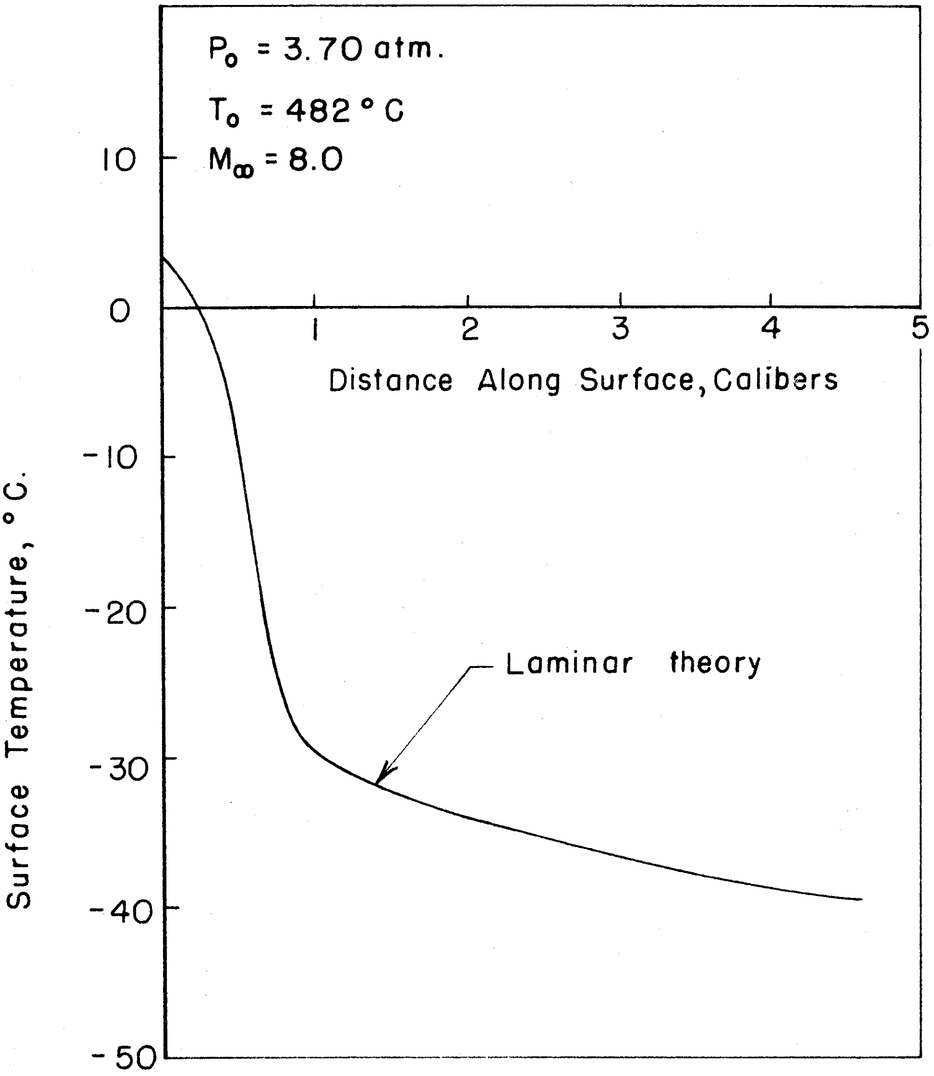

FIG.22 – SURFACE TEMPERATURE, H_2O-ICE

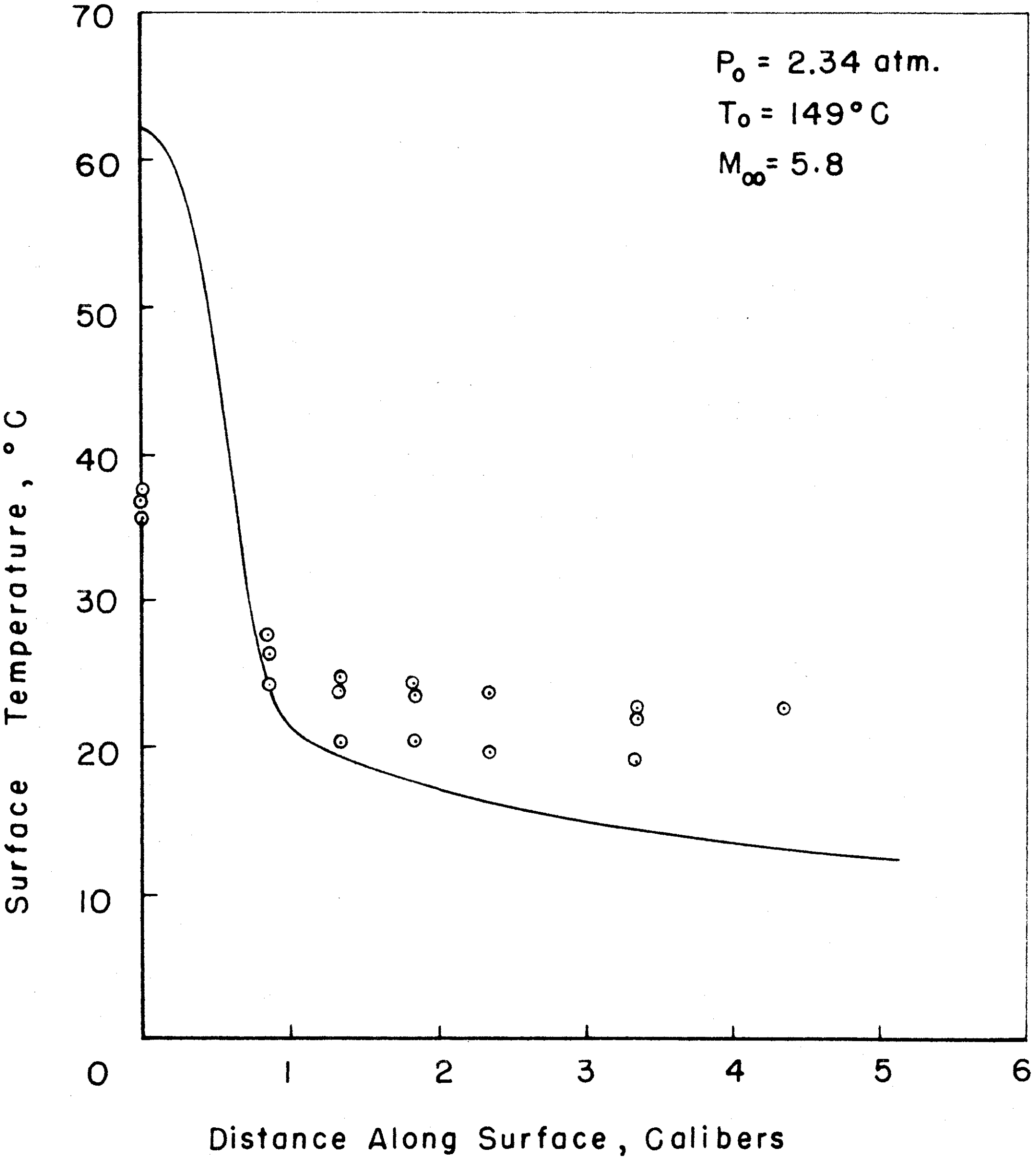

FIG. 23-SURFACE TEMPERATURE, $C_{10}H_{16}O$ - ICE

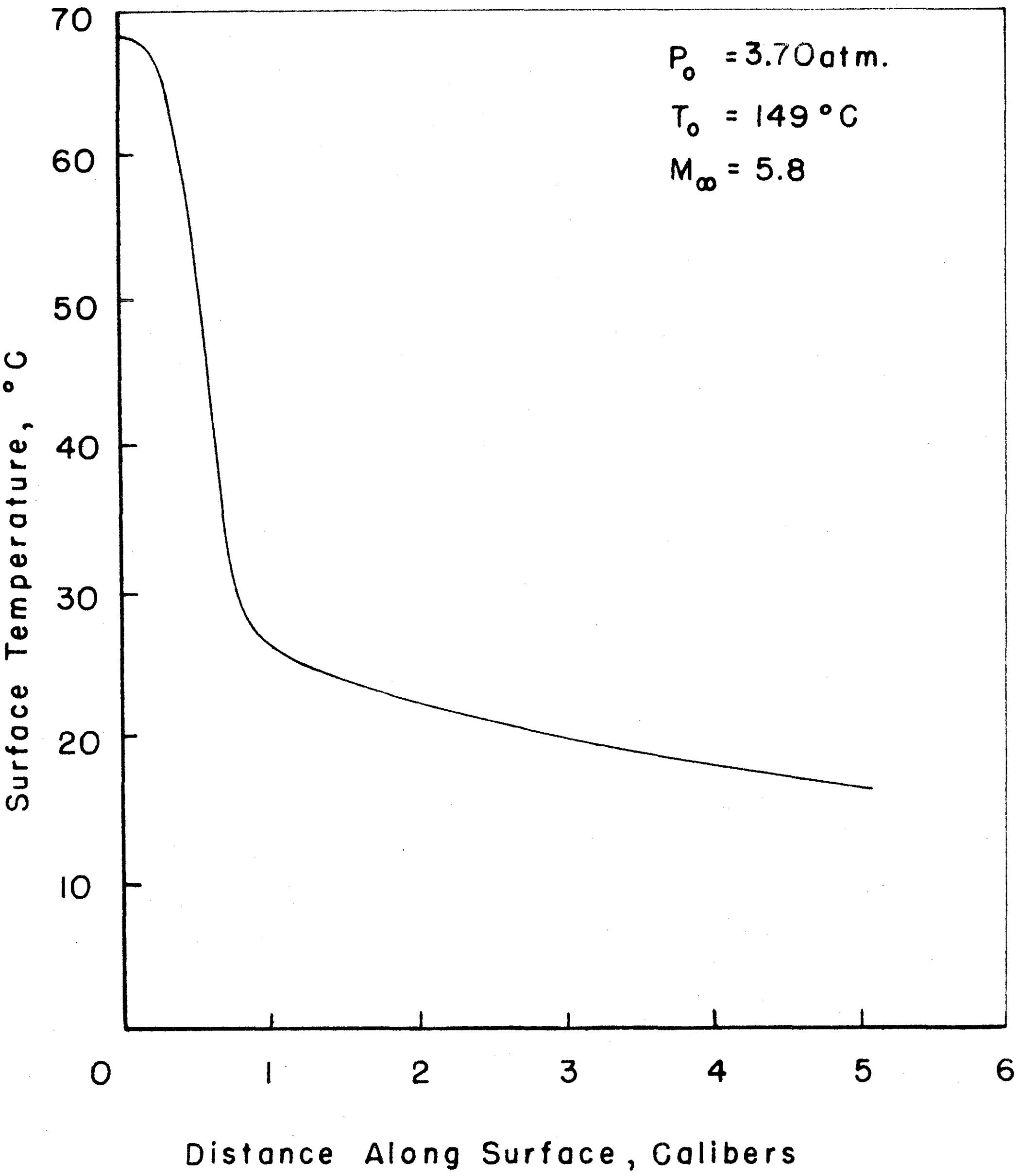

FIG. 24-SURFACE TEMPERATURE DISTRIBUTION, $C_{10}H_{16}O$-ICE

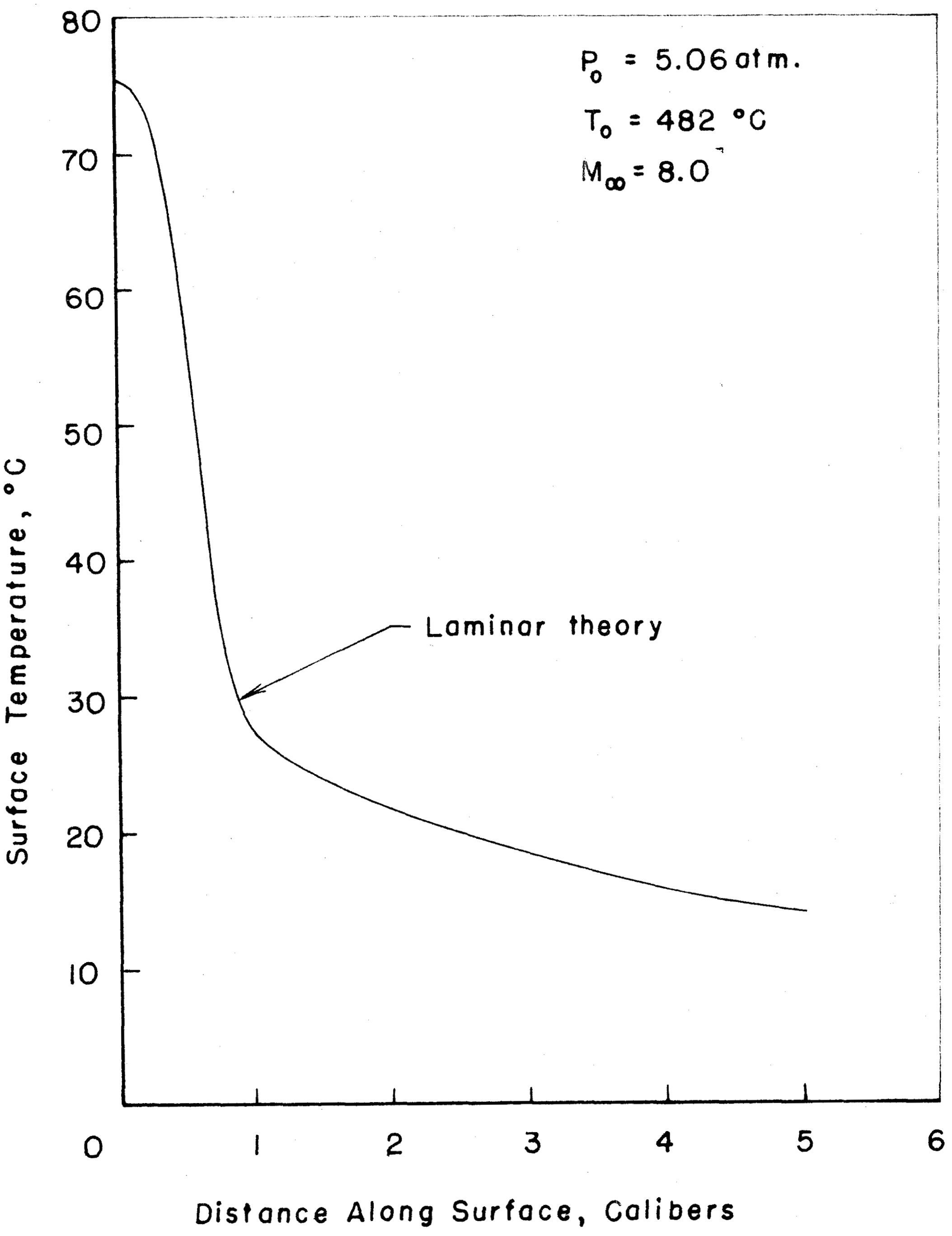

FIG. 25—SURFACE TEMPERATURE, $C_{10}H_{16}O$ – ICE

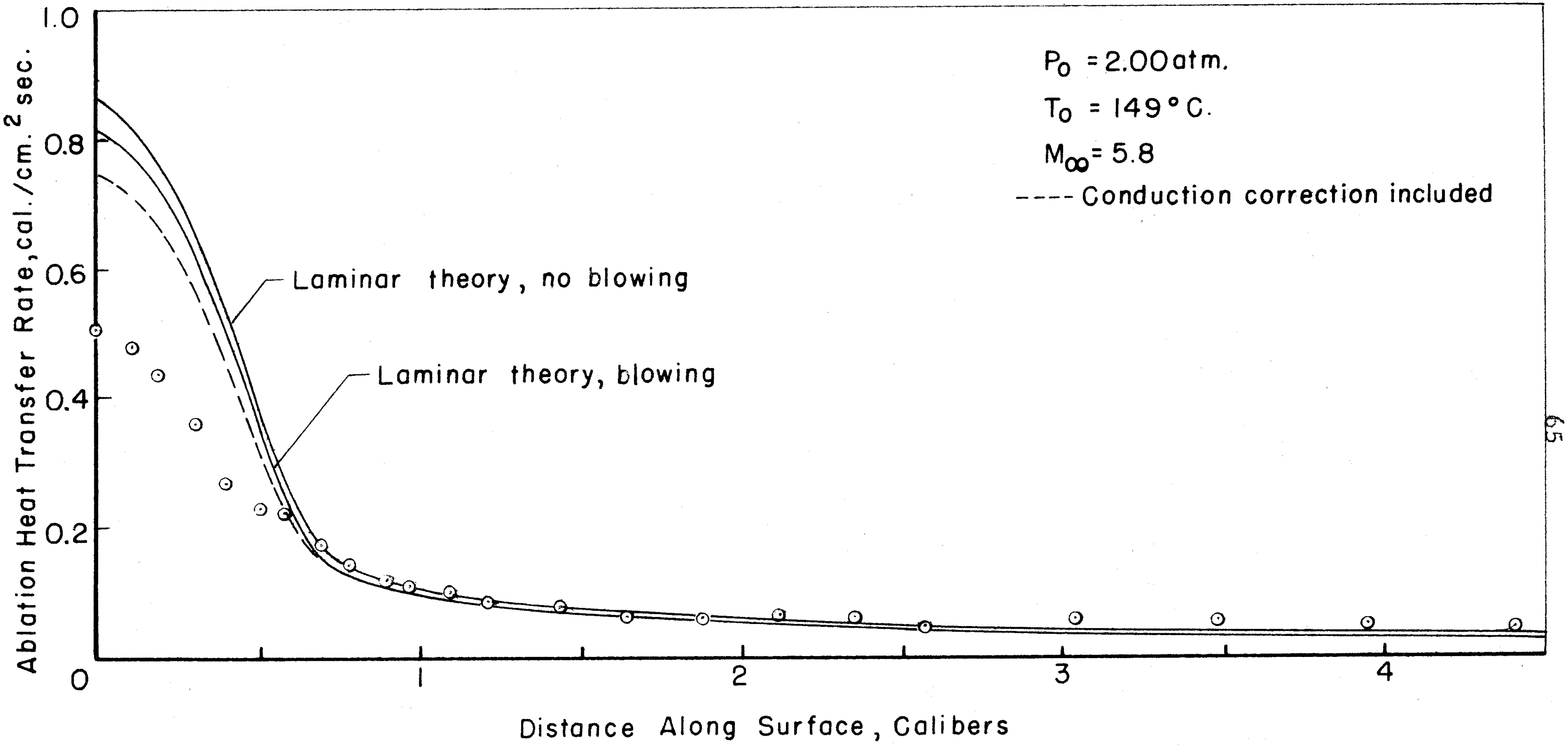

FIG. 26-ABLATION HEAT TRANSFER RATE ALONG SURFACE, H_2O-ICE

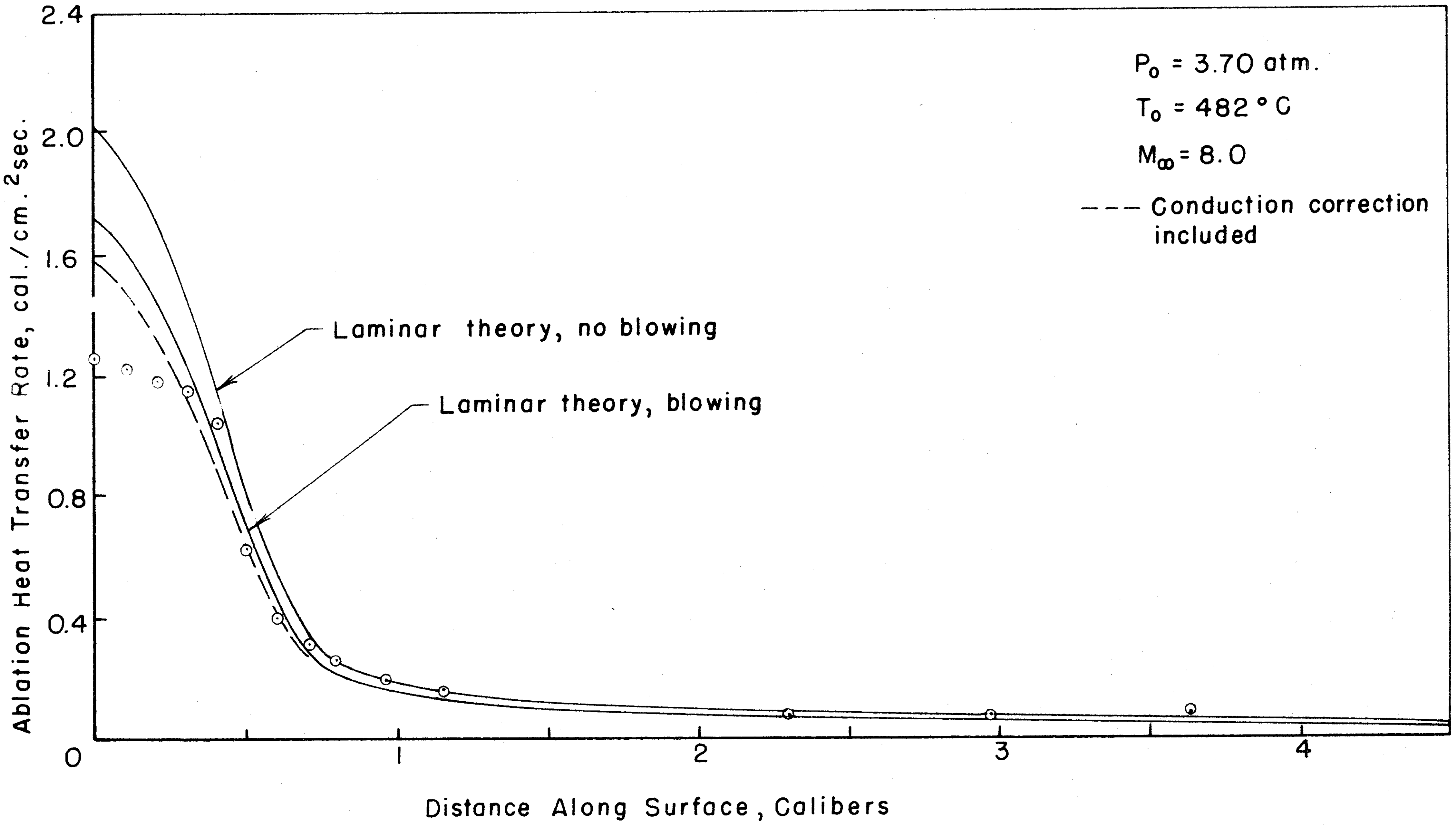

FIG. 27 - ABLATION HEAT TRANSFER RATE ALONG SURFACE, H_2O-ICE

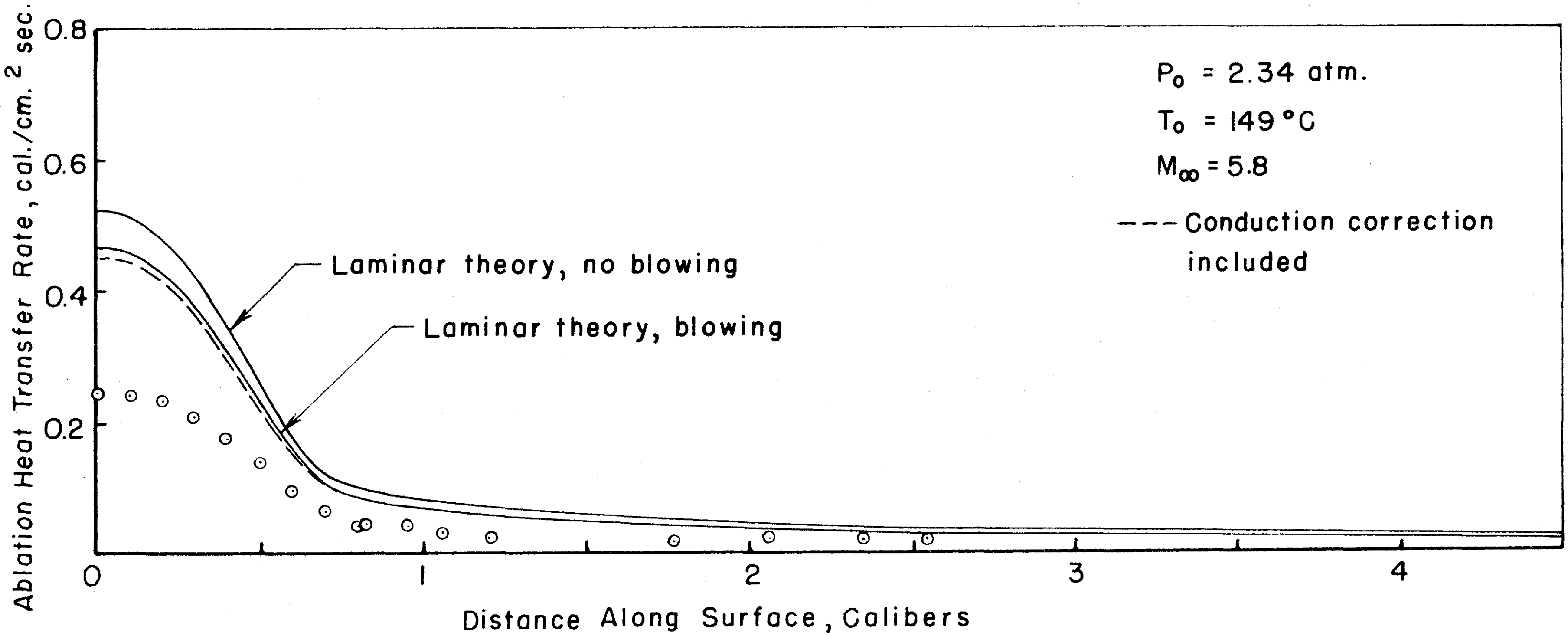

FIG. 28 - ABLATION HEAT TRANSFER RATE ALONG SURFACE, H_2O - ICE

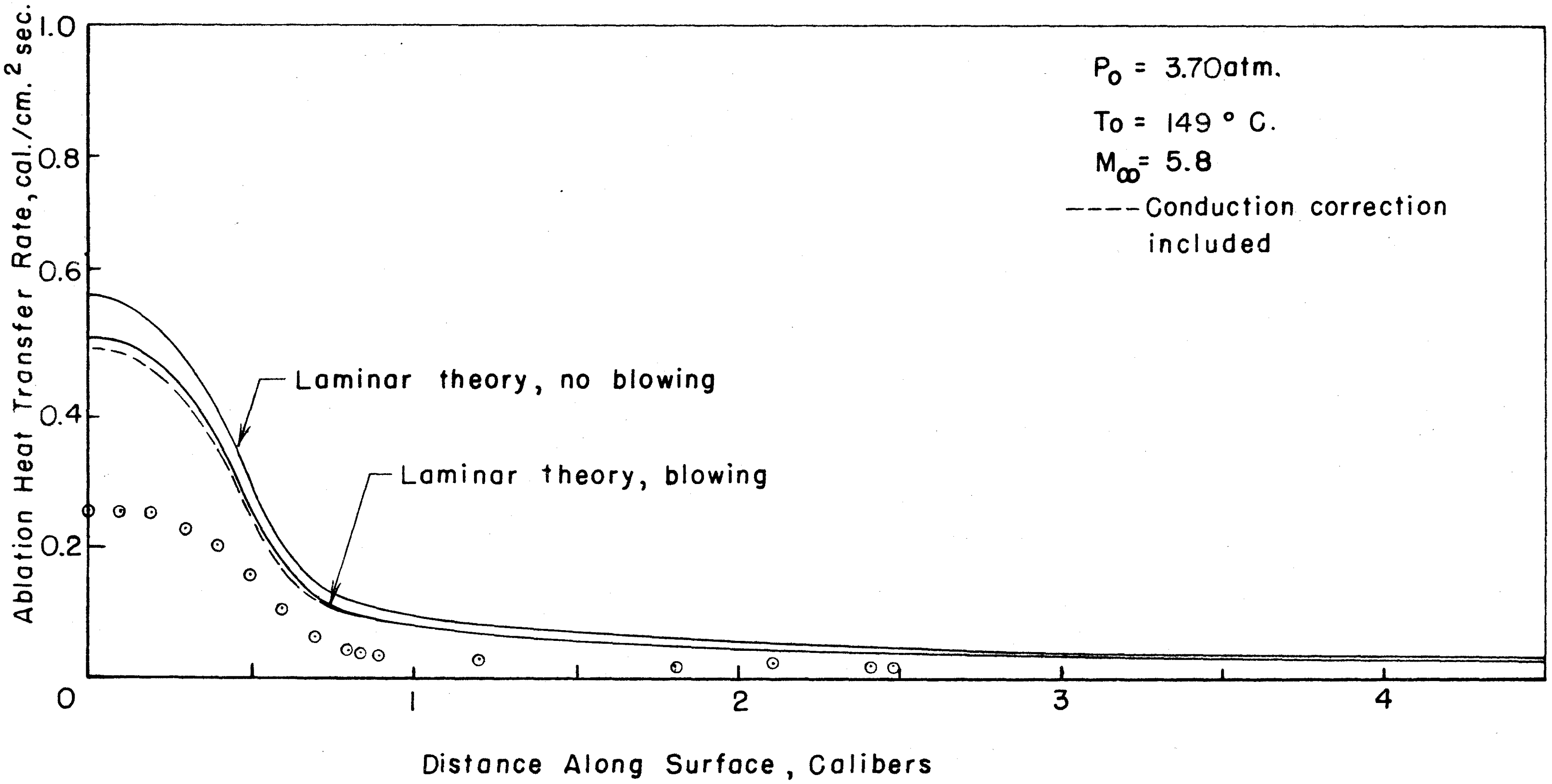

FIG. 29-ABLATION HEAT TRANSFER RATE ALONG SURFACE, $C_{10}H_{16}O$ -ICE

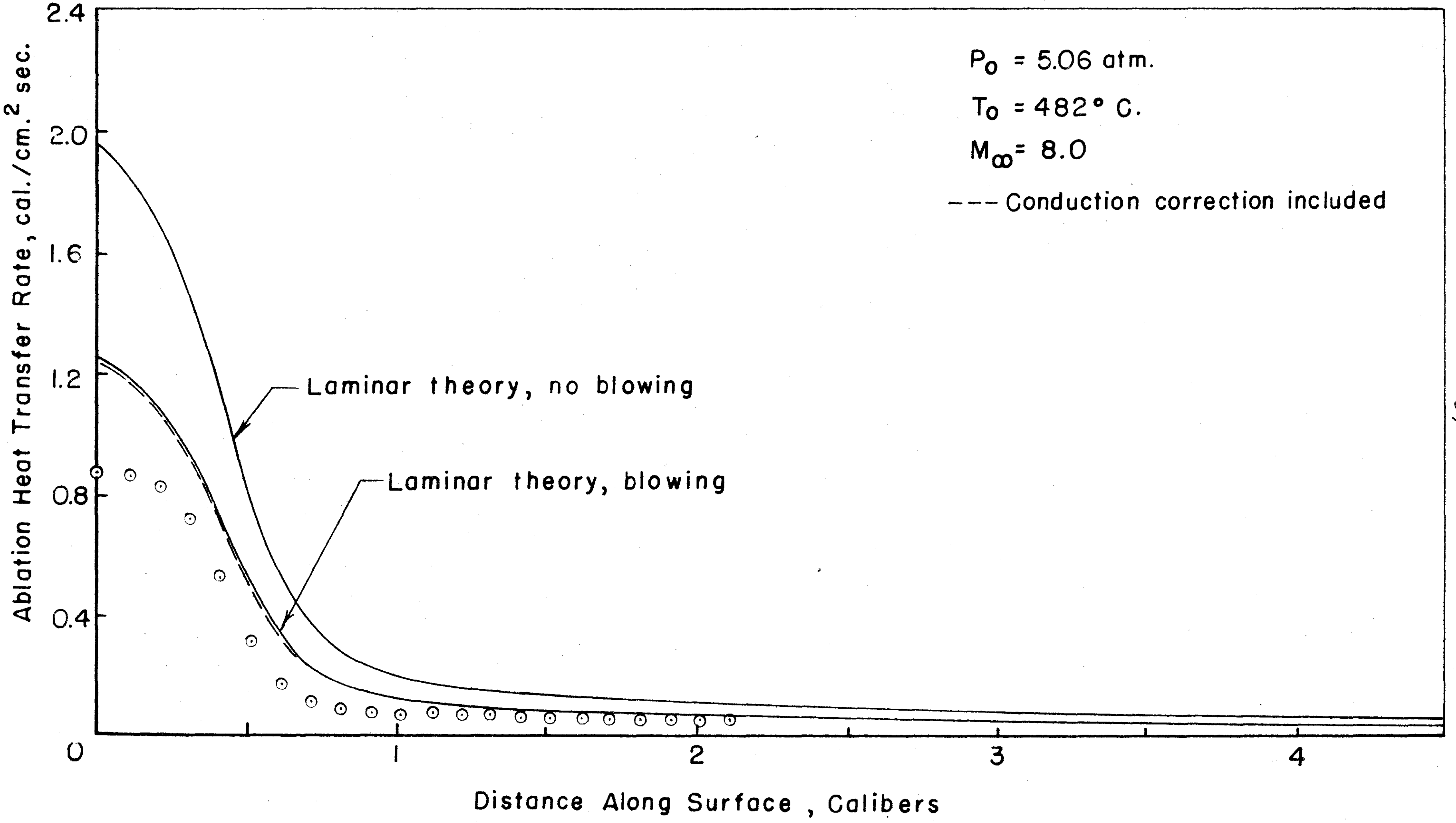

FIG. 30 - ABLATION HEAT TRANSFER RATE ALONG SURFACE , $C_{10}H_{16}O$ - ICE

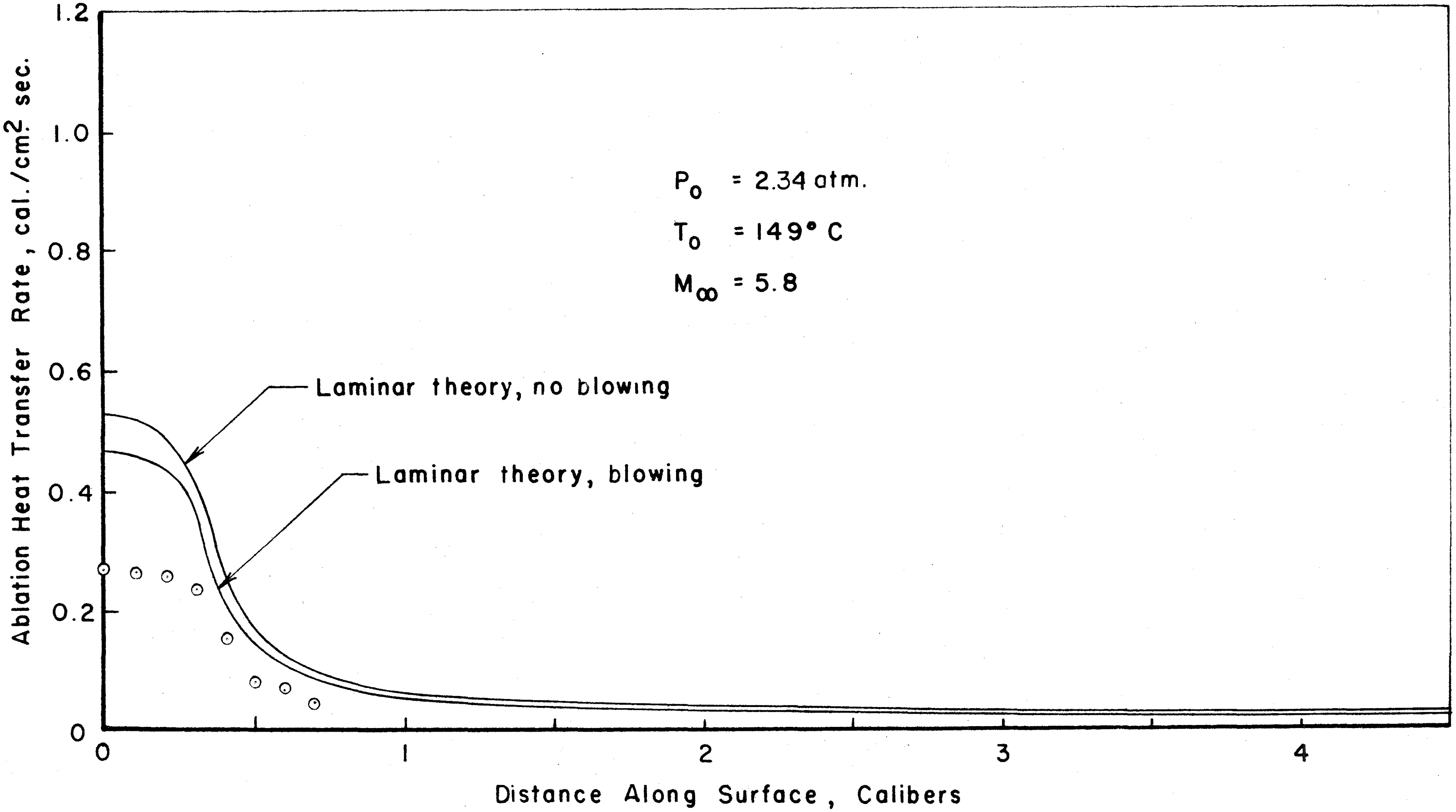

FIG. 31 -ABLATION HEAT TRANSFER RATE ALONG SURFACE, OF M_∞ = 5.8 EQUILIBRIUM-SHAPE MODEL, $C_{10}H_{16}O$ -ICE

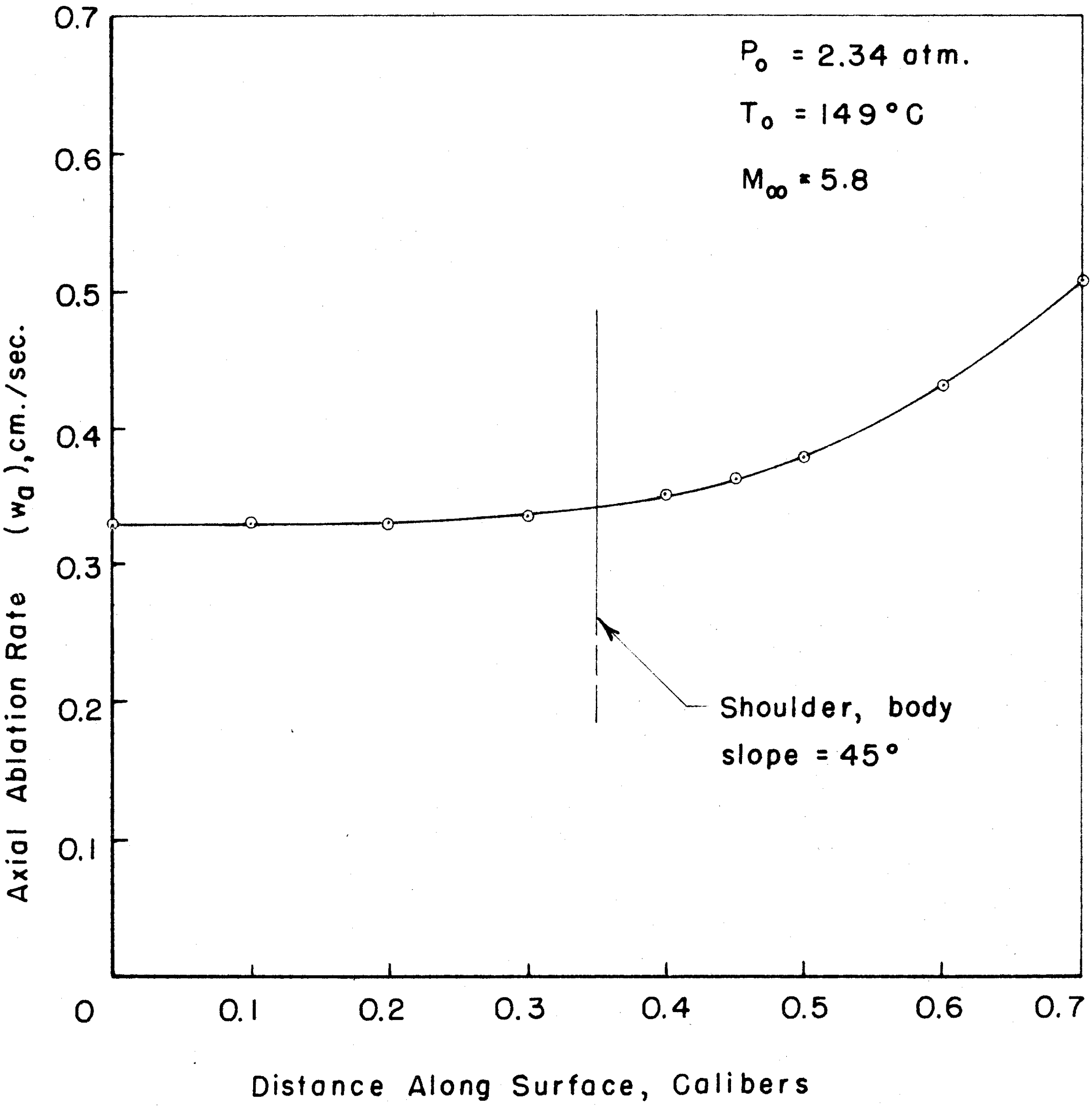

FIG. 32-AXIAL ABLATION RATE ACROSS THE NOSE AREA ON M_∞ = 5.8 EQUILIBRIUM-SHAPE MODEL, $C_{10}H_{16}O$-ICE